Femtosecond-laser hyperdoping and texturing of silicon for photovoltaic applications

Citation

Lin, Yu-Ting. 2014. Femtosecond-laser hyperdoping and texturing of silicon for photovoltaic applications. Doctoral dissertation, Harvard University.

Femtosecond-laser hyperdoping and texturing of silicon for photovoltaic applications

A thesis presented
by

Yu-Ting Lin

to
The School of Engineering and Applied Sciences
in partial fulfillment of the requirements
for the degree of
Doctor of Philosophy
in the subject of

Applied Physics

Harvard University
Cambridge, Massachusetts
May 2014

Thesis advisor	Author
Eric Mazur	**Yu-Ting Lin**

Femtosecond-laser hyperdoping and texturing of silicon for photovoltaic applications

Abstract

This dissertation explores strategies for improving photolvoltaic efficiency and reducing cost using femtosecond-laser processing methods including surface texturing and hyperdoping. Our investigations focus on two aspects: 1) texturing the silicon surface to create efficient light-trapping for thin silicon solar cells, and 2) understanding the mechanism of hyperdoping to control the doping profiles for fabricating efficient intermediate band materials.

We first discuss the light-trapping properties in laser-textured silicon and its benefit to thin silicon heterojunction solar cells. We report a nearly 15% improvement in the short circuit current and device efficiency after surface texturing, which is attributed to the enhancement of absorption due to the formation of Lambertian surfaces. We next present studies on the hyperdoping mechanism using a pump-probe method. We measure *in situ* the change in surface reflectivity during hyperdoping and extract the dynamics of the melt front. Understanding the melt dynamics allows us to constrain the physical parameters in a numerical model, which we use to simulate the doping profile with a simplified classical picture. We then demonstrate the successful fabrication of homogeneously doped silicon by manipulating the hyperdoping process based on theoretically predicted design principles.

Contents

Citations to previously published work

Parts of this dissertation cover research reported in the following articles:

1. B. G. Lee, Y.-T. Lin, M.-J. Sher, E. Mazur, and H. M. Branz, "Light-trapping for thin silicon solar cells by femtosecond-laser texturing," *IEEE Photovolt. Specialist Conference*, 2012.
2. B. G. Lee, Y.-T. Lin, E. Mazur, and H. M. Branz, "Light-trapping for thin silicon solar cells by femtosecond-laser texturing," *submitted to IEEE Journal of Photovoltaics.*
3. Y.-T. Lin, and E. Mazur, "Black silicon: history, methods, and photovoltaic applications," *soon to be submitted for publication in International Materials Review.*
4. Y.-T. Lin, G. Deng, and E. Mazur, "Mechanism of femtosecond-laser hyperdoping: an in situ pump-probe tudy," *soon to be submitted for publication in Applied Physics Letters.*
5. Y.-T. Lin, N. Mangan, S. Marbach, T. Schneider, G. Deng, M. Brenner, and E. Mazur, "How to achieve homogeneous dopant concentrations using femtosecond-laser hyperdoping," *soon to be submitted for publication in Physical review Letters.*

Acknowledgments

The past 6 years would have been impossible without each one of my mentors, colleagues, friends, and family, who have provided me with great supports and companionships. First, I'd like to thank Prof. Chun-Wei Chen who encouraged me to pursue a PhD degree at Harvard, which became the turning point of my life. I'm also grateful to receive so much caring and guidance from Prof. Chen throughout the years. Next I'm truly appreciated that Prof. Eric Mazur provided me with a chance to join his group, where I met countless talented and inspiring friends and colleagues. I was very lucky to have the freedom to pursue my own research goal with Eric's full support. The training Eric provided is extremely helpful for me to learn how to not only be a great scientist but also an effective communicator and educator. I'd also like to thank my committee members: Mike Aziz, Evelyn Hu. Particularly, I really appreciate Mike for sharing his knowledge and wisdom with me over the years.

In the Mazur group I was fortunate to have worked with many great scientist. Mark Winkler was my first mentor who taught me how to survive in the cleanroom. Paul Peng guided me through the hardest time when I began to learn about pump-probe. I miss those moments when I came early in the morning and saw Mark sleeping on the couch or Paul coming back from the gym. I want to also thank Renee Sher who was always there to provide support when I was puzzled or needed suggestions in the past few years. I'd also thank Chris Evans for sharing with me his knowledge in optics. Of course I won't forget Tina Shih, Eric Diebold, Jason Dowd, Sam Chung, Kevin Vora, Prakriti Tayalia, Jessica Watkins who introduced me to the Mazur group spirit when I joined 5 years ago. I want to particularly thank Guoliang Deng who had been a great cowork for two years. We spent many early mornings and late nights running experiments and brainstorming ideas. I'm also really grateful to have Kasey Philips, Ben Franta, Kelly, Miller, Laura Tucker, Julie Schell, Michael Moebius, Phil Munoz, Orad Reshef, Francois Parsy, Jin Suntovich, Jon Bradley, Sarah Griesse-Nascimento, Nabiha Saklayen, Alex Raymond, Hemi Gandhi Haifei Zhang, and Sebastien Courvoisier, Daryl Vulis, Marinna Madrid, and Li Yang for your friendship and company. Also, I enjoyed interacting with many visitors in the group including Thierry Sarnet, James Fraser, Erwin Marti, Michelle Munier, James Fraser, and Ping Zhang. Finally, I would like to give special thanks to Virginia for always taking care of the details of the lab patiently and being the friendliest person in the world.

I'd like to thank Sally Kang for being an amazing friend for the past few years. We've gone through many ups and downs together since our first year. It would have been impossible for me to see this day coming without Sally's companionship. I am really glad that we are completing this journey together. Valeria Nuzzo was also a really good friend who is like a life mentor to me. I enjoyed every moment chatting and hanging out with Valeria and her family, especially the cute little Mila, either in Boston or Paris. I also enjoyed two great summers mentoring Weilu Shen and Richard Hampton. It was a great pleasure working with Weilu, who is also a great friend who introduced me to the world of Snapchat. Her passion brings sunshine to the basement of LISE, where we spent much time FIB-ing TEM samples.

I also had a chance to collaborate with many different research groups around the world. First I will thank many of the professors I have collaborated with including Prof. Tonio Buonassisi, Prof. Silvija Gradecak, Prof. Michael Brenner, Prof. Au-

gustinus Asenbaum, Prof. Giancarlo Salviati, Prof. Wei-Fong Pong, Prof. Ya-Ping Chiu. I would like to thank Benjamin Lee and Howard Branz at NREL for collaborating on the light trapping solar cell project. Niall Mangan and Sophie Marbach were very productive collaborators on the hyperdoping project. I want to particularly thank Tobias Schneider for not only being a really dedicated collaborator but also an awesome friend. Matt Smith did fantastic analysis on our black silicon sample. I am grateful to have been working with Filippo Fabbri who is also an amazing microscopist and a true friend who shares the same taste in music with me. I enjoyed every concert we went together and I look forward to many more to come. And I thank Sz-Chang Chen for many fruitful discussions on synchrotron analysis via skype.

I want to thank Rachel, Marcus, Ethan, and Nanyan for being supportive friends for the past few years. It is your company that recharges my battery when I am away from the lab. I want to thank all my friends in Taiwan who I miss everyday even when I am far away. Dachura and Yuching, thanks for always being there to care and share with me things I am missing out in Taiwan. Lastly, I would like to give a huge acknowledgement to my parents for always having trust in me and giving me the freedom to pursue my dreams. Your endless love and support is what I carried wherever I am far away from home. I'm proud of myself only when realizing I've succeeded in making you proud. The ending of my PhD career is just a start for another chapter in my life. I will continue to do my best to make you proud.

Acknowledgements of Financial Support

This thesis is based on work funded by the National Science Foundation under contract CBET-0754227 and DMR-0934480.

To my loving family

Chapter 1

Introduction

1.1 Overview

Femtosecond-laser processing provides new outlooks to the solar industry through two aspects: surface texturing and hyperdoping. Surface texturing enhances the absorption efficiency of a material and enables a reduction in active layer thickness without sacrificing the device efficiency. Hyperdoping changes the band structure of a material and allows absorption of sub-bandgap photons. Both approaches grant promises towards achieving highly efficient and low cost solar cells. In this dissertation, we first present a successful implementation of our laser texturing technique to fabricate light-trapping thin silicon solar cells. We then discuss our fundamental understanding of the hyperdoping mechanism and demonstrate the feasibility to design and fabricate hyperdoped silicon on demand.

1.2 Organization of the dissertation

In chapter 2, we review the history of black silicon, various fabrication methods, and the state-of-the-art solar cells based on each types of black silicon. We also introduce the idea of light-trapping and its importance to thin silicon solar cells.

In chapter 3, we present efficient light-trapping silicon surfaces made by femtosecond-laser texturing. We then demonstrate an improvement in the external quantum efficiency, the short circuit current and the device efficiency in heterojunction solar cells made of our laser-textured material.

In chapter 4, we elucidate the underlying mechanism of femtosecond hyperdoping of sulfur in silicon. We develop a pump-probe technique to probe the change in surface reflectivity during the hyperdoping process and extract the melting and resolidification dynamics.

In chapter 5, we design and fabricate homogeneously hyperdoped silicon based on our understanding of the hyperdoping mechanism.

In chapter 6, we summaries the work in this dissertation and provide suggestions to future studies.

Chapter 2

Progress in photovoltaics: black silicon and light-trapping solar cells

2.1 Introduction

Silicon is the second most earth-abundant element and the most used semiconductor in the solar industry. Notably, crystalline silicon solar cells share about 85% of the market due to the materials excellent properties [1]. First of all, silicon can be easily purified because most of the notorious efficiency-reducing impurities have low solid solubility in crystalline silicon [2]. Secondly, silicon can be doped both n-type and p-type to form p-n junctions. Furthermore, silicon oxidizes naturally to form a thin passivation layer that prevents the device from degrading. Stability of the material allows a warranty of 80% device performance even 25 years after the installation [1].

The first crystalline silicon solar cell was made almost 60 years ago, with an efficiency of 6% [3]. Over the decades, robust research and development continue to thrive. With the great technology transfer from the laboratory to industrial production, commercial cystalline solar cell has an efficiency of 25% at a steadily declining cost [1]. To become competitive in the U.S. without subsidies, the cost of crystalline silicon solar cells has to reduce to 0.5-0.75 dollars per Watt at its peak power (USD/Wp). This means we need to cut half of the current production cost. Two of the main strategies to achieve this milestone are to increase the device efficiency and reduce the feedstock cost. For enhancing efficiency, the first step is to maximize the material's absorption by reducing the reflection loss at the surface. The idea of making silicon "black" thus has become one of the main research topics in the past few decades. For reducing the feedstock cost, it is intuitive to make the active layer thinner. However, how to manage the sunlight so that most energy is absorbed within a thinner material becomes another challenging and interesting field of engineering.

In this chapter, we first review various kinds fabrication methods to produce "black silicon". We will then introduce "light-trapping" as an important engineering route that greatly enhances the absorption in thin silicon solar cells.

2.2 Black silicon for photovoltaic applications

2.2.1 Overview

The formation of silicon needles or pillars, known as "grass" or "black silicon", was first discovered in the 70s as an undesirable side effect during the reactive ion etching (RIE) process [4–7]. Figure 2.1 shows the surface morphology of an RIE-made grass/black silicon. Although many researchers were finding ways to solve this roughening problem, some later found out the undesirably surface structures could actually be beneficial for photovoltaic devices where minimizing reflection is crucial to enhance the energy conversion efficiency. [4, 8]. Figure 2.2 compares the reflectivity of a grass surface to a flat silicon reference [9]. The reflectivity of grass is nearly zero across the visible and near infrared spectrum. This is due to the fact that these nanostructures are much smaller than the wavelength of light. When light is incident on the surface of grass, it is effectively traveling through a medium that has a graded index of refraction. Consequently, instead of reflecting as usual at an interface of two mediums of different refractive index, light can now enter the grass with minimum reflection [10].

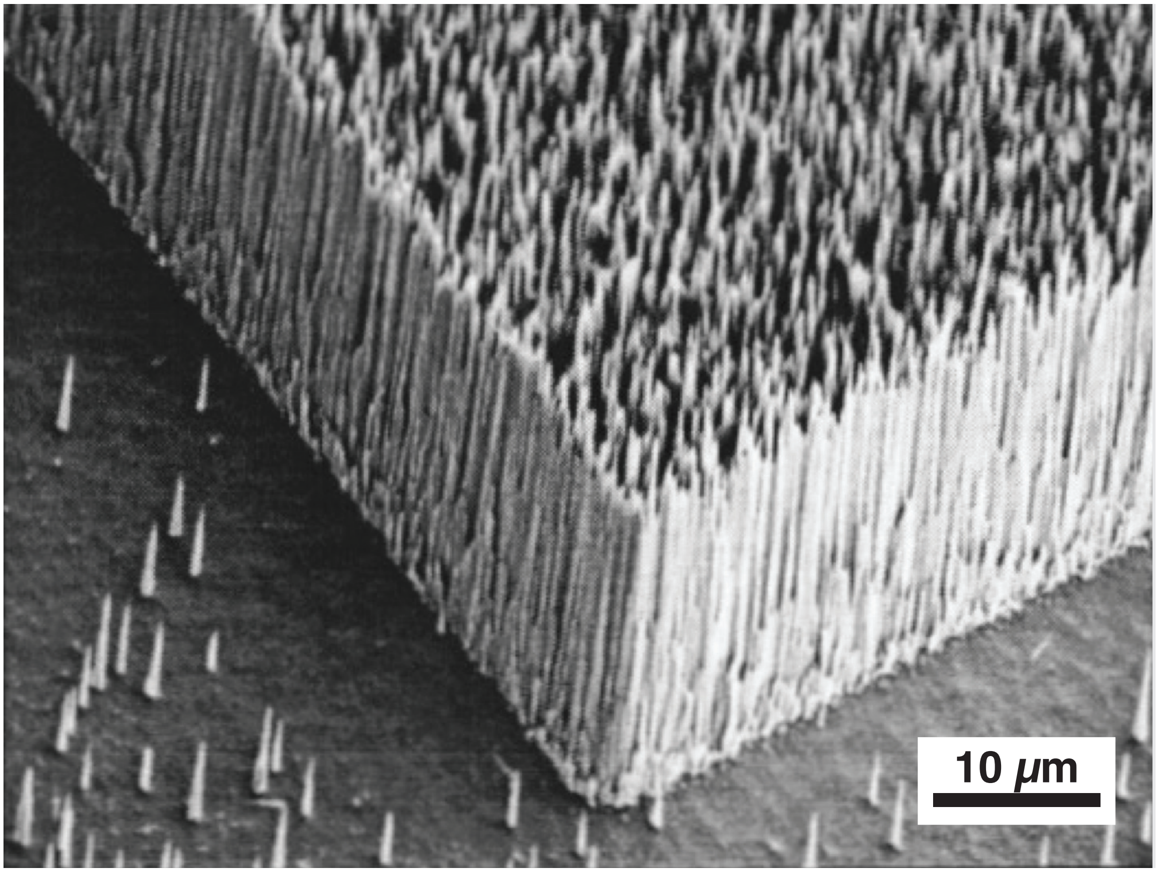

Figure 2.1: A SEM image of grass/black silicon made by RIE. The image is adapted from reference [11].

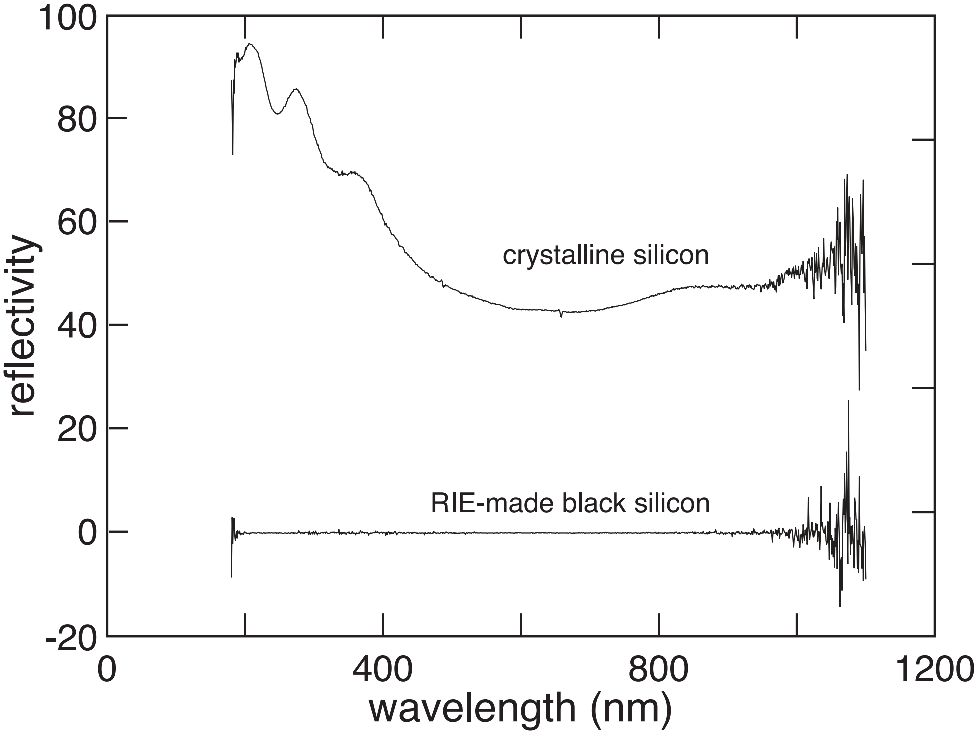

Figure 2.2: Normal incidence spectral reflectance of a RIE-etched black multicrystalline silicon surface and a polished multicrystalline silicon surface. Data adapted from reference [9].

Randomly texturing the silicon surface with KOH solution has been a standard industrial procedure for creating an antireflection and light-trapping surface in a solar cell [12]. KOH has anisotropic etch rates to silicon, particularly slow on the (111) plane in silicon [13]. Thus, pyramid like structures form on the silicon surface after etching with KOH. However, this method does not work well for multicrystalline silicon where the crystal orientation varies from grain to grain. Efforts in making black silicon therefore focus on methods that are not selective to the crystal orientation for applications on cheap multicrystalline silicon.

Researchers have investigated various methods to create black silicon in addition to RIE, such as: porous silicon etching [14], mechanical diamond saw cutting [15], photolithography-defined etching [16], metal-assisted etching [17], and laser texturing [18]. In this chapter, we discuss two black silicon methods including RIE and laser texturing. There are several advantages of these two black silicon methods. For example, they requires no pre-patterning; they can texture a large area efficiently; and they are applicable to silicon of any crystallinity and even other material systems such as metal and dielectrics [9, 19–23].

2.2.2 Reactive ion etching

RIE is one of the standard semiconductor microfabrication techniques. The RIE system consists of a vacuum chamber, electrodes, and a gas flowing system. The chosen gas species typically react with the targeted material to form volatile products that leave the system easily. For example, SF_6 and CCl_4 are common gases for etching silicon because the reaction products, SiF_4 and $SiCl_4$, are volatile [11]. In a RIE process, a strong radio frequency (RF) electromagnetic field generates plasma by stripping off the electrons from the ions of the flowing gas molecules. The highly mobile electrons build up at the DC-isolated platter electrode, resulting in a strong electrical field on the order of a few hundred volts. The heavy ions thus tend to accelerate towards the sample surface and bombard the surface with high kinetic energy. As a result, there are two effects concurrently etching the sample: 1) chemical reaction between the active ions and the sample surface, and 2) physical sputtering via momentum transfer from the directional bombarding ions to the surface atoms. The former process is isotropic while the later process is the key for achieving an anisotropic etching.

Therefore, the relative etching rates between the chemical reaction and physical sputtering determines whether the etched wall is straight or tapered. For example, it is possible to achieve a deep straight trench etching by quenching the chemical reaction with cryogenic processes or passivation of chemically inert molecules [11, 24, 25].

Surface roughening during the RIE processes is a common phenomenon in different materials systems such as silicon, SiO_2 and, polymer [26–28]. Although there were debates about the formation mechanism, it is now widely accepted that these structures result from the micromasking effects in the highly selective RIE process. The masking materials could be native oxide and dust on the surface, redeposition of the pre-existing masking materials such as SiO_2, and involatile surface residues formed by interaction of reactive plasma species with the electrode material [5–7, 29]. The surface features of the RIE-made black silicon are controllable by altering the gas species, the reaction pressure and the RF power [7, 8, 30, 31]. The gas species and processing pressure determine the amount of inhibitor adsorption on the surface. The RF power controls the accelerating voltage of ions and thus affects the amount of mask redeposition. Inomata *et al.* demonstrated controllability of aspect ratio of the surface structure by changing the Cl_4 flow ratio [32]. Figure 2.3 shows a variety of surface morphologies made by RIE with SF_6 and O_2 plasma [31].

For photovoltaic applications, it is important for a material to have not only strong absorption but also efficient carrier transport properties. Researchers found that although the RIE-etched silicon surfaces have perfect antireflection, the concurrently generated surface damage due to ion bombardment limits the electronic performance of this roughened material [33]. Practically, this problem is solvable by

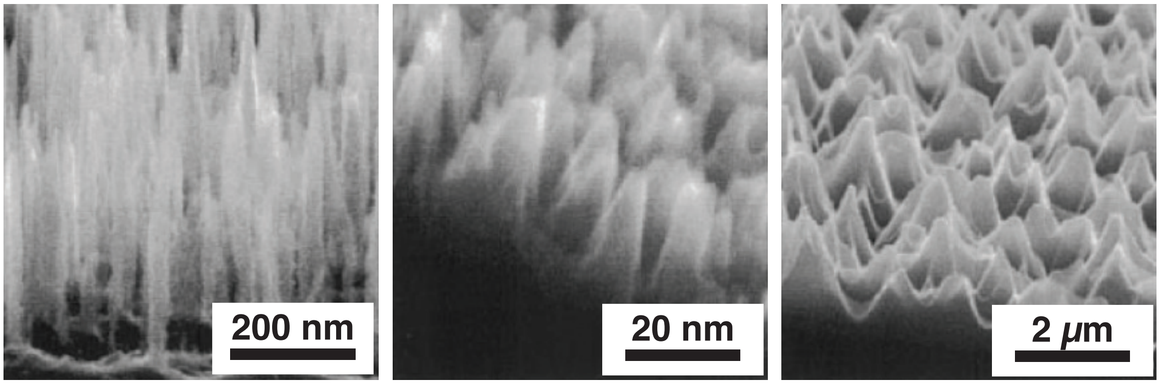

Figure 2.3: SEM pictures of different types of RIE-etched silicon surfaces: (Left) grass, (Middle) pillars, (Right) pyramids. Different structures can be made by tuning the SF_6 and O_2 flow ratio. Images adapted from reference [31].

applying an additional damage removal etching process to recover the material quality while maintaining the antireflection property [9,33,34]. Yoo *et al.* have demonstrated a 16.1% energy conversion efficiency of a 200-μm multicrystalline silicon solar cell using RIE and damage removal etching [34]. Their RIE-textured device has an enhanced short circuit current as expected from a better antireflection property of the surface. Recently, Repo *et al.* reported an 18.7%-efficient RIE-made black silicon solar cell. The key to their success is to passivate the black silicon surface with a 10-nm layer of Al_2O_3 by plasma-assisted atomic layer deposition. The passivation improves the internal quantum efficiency at short wavelengths, suggesting a suppressed surface recombination [35, 36]. Although some of the RIE-textured surfaces reported in the literature appears to be perfect randomized, most of the discussion focus on the material's antireflection properties rather than light-trapping [9,33,34,37,38]. However, we note that light-trapping could play a role in the enhanced absorption for some of the RIE-generated structures having randomly distributed wavelength-sized landscapes.

2.2.3 Laser texturing

The Mazur group discovered another type of black silicon by irradiating silicon with a train of femtosecond-laser pulses in a SF_6-containing atmosphere [39]. The flat silicon surface transforms into conical morphologies after multiple laser irradiations as seen in Figure 2.4 (Left) [40]. Interestingly, the laser-induced surface roughening is also an undesirable effect during pulsed-laser deposition. However, a photolvoltaic device can utilize the enhanced absorptance across the visible and the infrared spectrum as shown in Figure 2.4 (Right) [41].

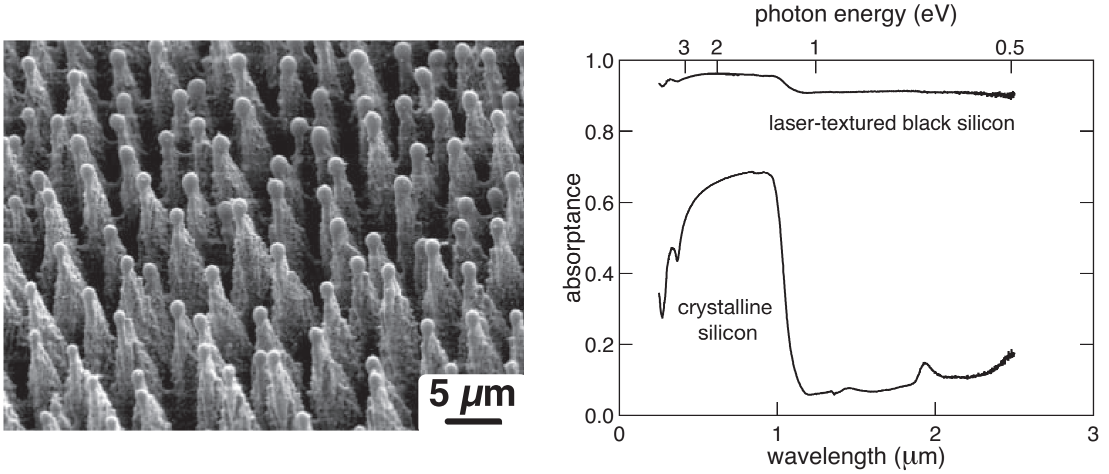

Figure 2.4: An SEM image of a laser-textured black silicon [40], and (Right) the absorption spectrum of laser-textured black silicon compared to a flat crystalline silicon [41].

We can attribute the enhanced absorption in the visible spectrum to geometric factors. The textured-surface has a larger size and spacing than the visible wavelength. Considering light normally incident on laser-textured black silicon, it bounces between the valleys on the surface and has multiple chances of entering the material. This results in a strong antireflection effect in a similar way as the KOH-etched pyramidal structures [12, 42]. The geometric antireflection is a function of the cone angle. Figure 2.5 compares the geometric effect in a laser-textured black silicon to a KOH-etched silicon surface. The light paths are predicted by assuming both the laser-textured and anisotropically etched surfaces have a refractive index of 4 for light having a wavelength of 600 nm. Our laser-textured surface has a smaller cone angle and larger aspect ratio than the KOH-etched surface structures. Consequently, the incident light bounces a few more times between the laser-made cones before escaping the surface compared to the case in the chemically etched pyramids, leading to a higher absorption enhancement. Furthermore, light enters the material with an angle and experience total internal reflection when hitting on subsequent interfaces. In this case, light is essentially trapped inside the material via geometric light-trapping, which we will in the next section [12].

The formation of the spiky black silicon surface consists of several steps. First, laser-induced periodic surface structures (LIPSS) in the shape of ripples generate on the surface after the first few laser shots [43, 44]. Sipe *et al.* developed a widely accepted theory that attributes the ripples to frozen surface waves during fast solidification induced by the laser irradiation. These surface waves form as a result of uneven energy deposition and variation in the melt depth due to interference between the incident light and the scattered light at the surface [45]. These structures are expected to have spacing on the order of the laser wavelength for the interference effect. Another speculation is that surface plasmon polaritons play a role in the uneven energy deposition [46,47]. Bonse *et al.* incorporated the Drude model into Sipe's theory to explain the orientation and spacing of LIPSS at various energy deposition [48–50].

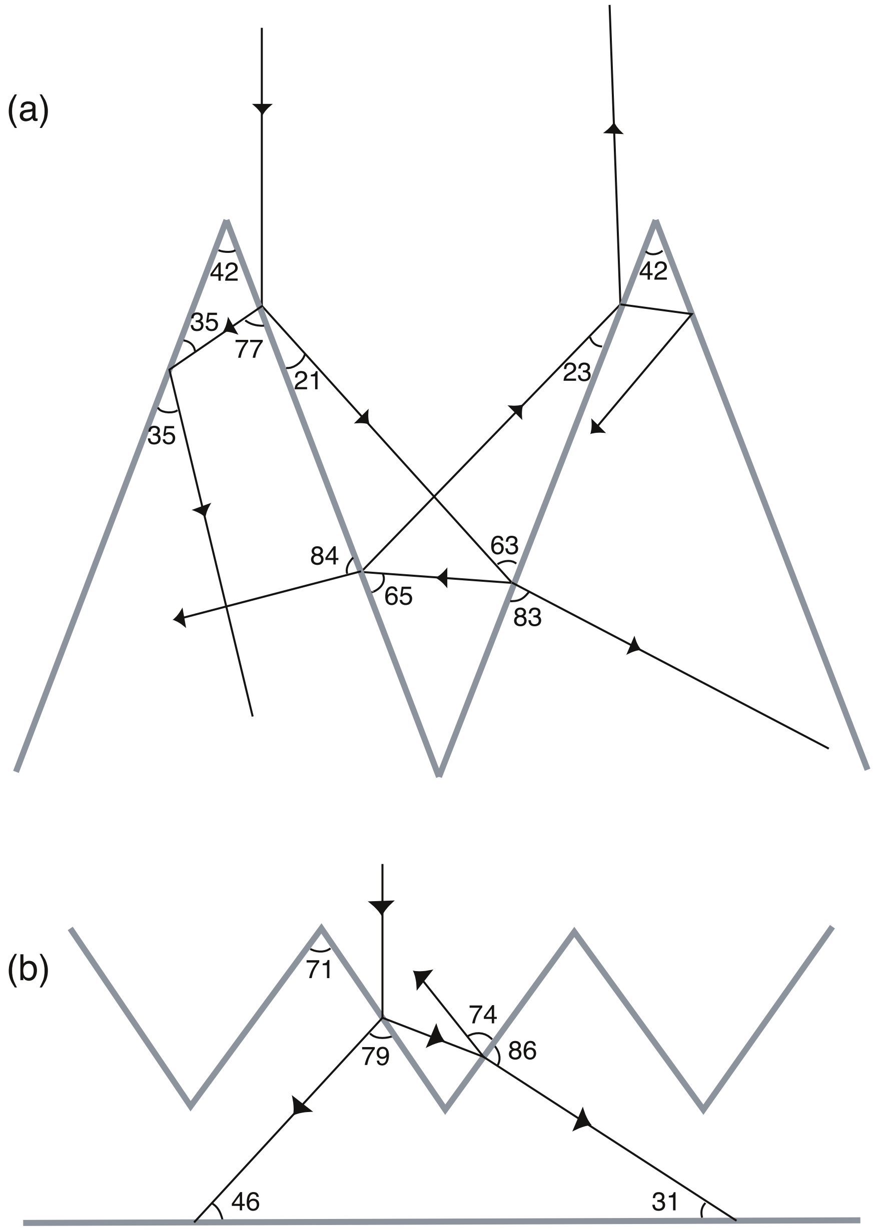

Figure 2.5: Illustration of the optical path of light incident on microstructured silicon surface: (a) Our laser-textured surfaces, with cones subtending 42°, (b) Textured silicon surface of pyramids made using anisotropic chemical etching. Angles are labeled in degrees. Adapted from reference [42].

The surface ripples tend to collapse and form beads with increasing laser irradiations or higher laser fluence. Recurring feedback further enhances uneven energy deposition. As a consequence, the beads grow into pillars and cones of variable periodicity and height depending on the laser parameters. Figure 2.6 shows an SEM image of a silicon surface irradiated by femtosecond-laser pulses in air for 500 shots [42]. The Gaussian nature of the pulses results in stronger energy deposition in the center compared to the periphery. We observe different structures including ripples, beads and cones with increasing energy deposition.

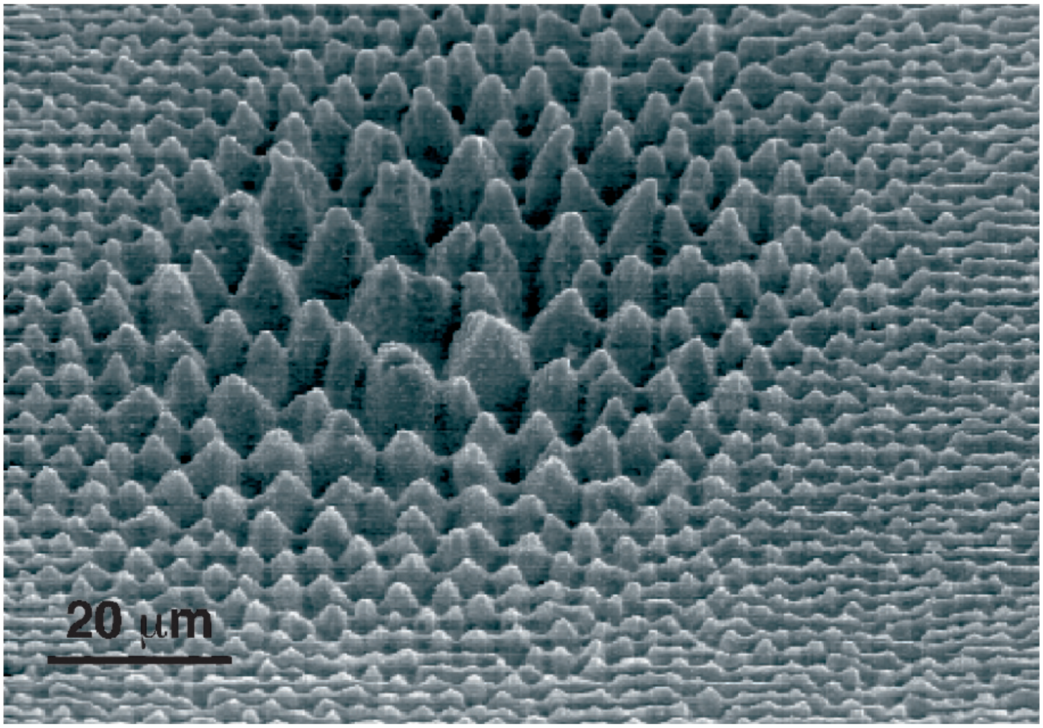

Figure 2.6: A SEM image of silicon microstructures made in air by irradiating silicon with 500 pulses, with 245 mJ per pulse, without translating the laser beam. Note the ripple-like structure around the periphery of the patterned area [42].

We can control the surface structures with processing parameters including the laser fluence, the shot number, pressure, and the ambient gas species. As shown in Figure 2.6, a higher the fluence results in larger surface structures with bigger spacing. In Figure 2.7, we see the surface structure evolution with increasing laser irradiations from 0 to 300 shots in a SF_6-atmosphere [51]. Similar to the RIE process, SF_6 molecules react with silicon to form a volatile gas SF_4 during the texturing process. Therefore, the etching effect makes the surface cones sharp in shape. By tuning the amount of SF_6 in the environment during laser texturing, we can produce various surface structures. Figure 2.8 shows a series of laser-textured silicon surfaces made in different SF_6 pressure with the same laser fluence and shot number. In vacuum (Figure 2.8 (a)), there are no gas molecules providing pressure to the silicon surface during melting and resolidification in each laser irradiation cycle. The surface structures generated in vacuum are thus bigger compared to other cases. When we increase the SF_6 pressure from vacuum to 5 torr (Figure 2.8 (b)), the size of the surface cones becomes smaller in height. Ridges form on the surface between an SF_6 pressure of 20 to 300 torr (Figure 2.8 (c)-(e)). The ridges are skinnier at higher SF_6 pressure. At 500 torr, cones that are much sharper than the case in vacuum appear on the surface. Increasing the pressure from 500 torr to 750 torr does not affect the surface morphology [52]. We conclude two effects determining the size and shape of the laser-induced surface structures. First, a higher SF_6 pressure results in taller and sharper structures due to the etching effect. Second, ablation occurs more easily at lower pressure, resulting in larger structures. We note that other chemically active gases such as Cl_2 also produces sharp structures in addition to SF_6 [42].

In addition to the geometric effect that enhances absorption in the visible spectrum, the sub-bandgap absorption also approaches unity in black silicon made by

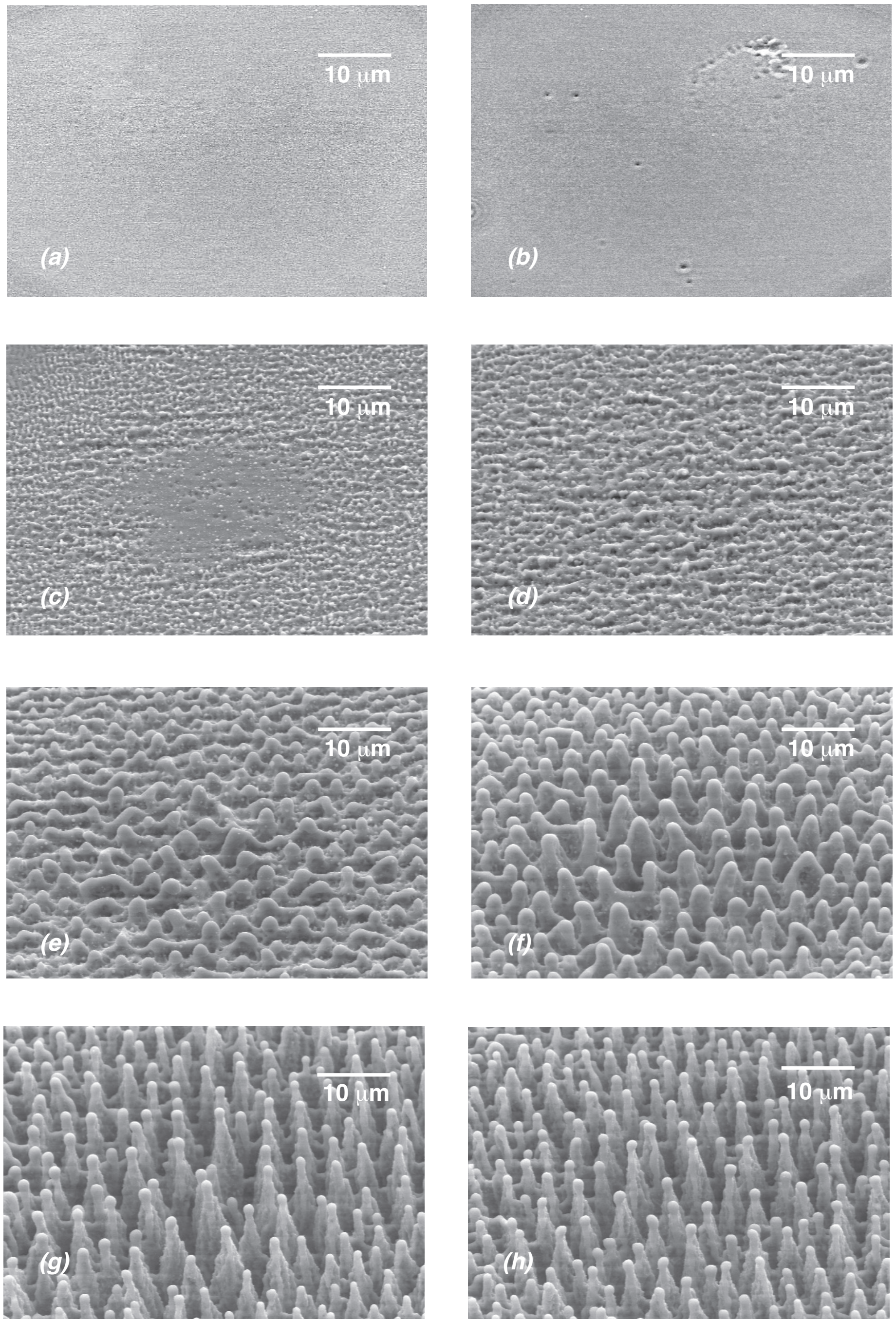

Figure 2.7: Silicon surfaces after (a) 0 pulses, (b) 1 pulses, (c) 5 pulses, (d) 10 pulses, (e) 25 pulses, (f) 50 pulses, (g) 150 pulses, and (h) 300 pulses of 10 kJ/m^2 fluence in 500 torr of SF$_6$ [51].

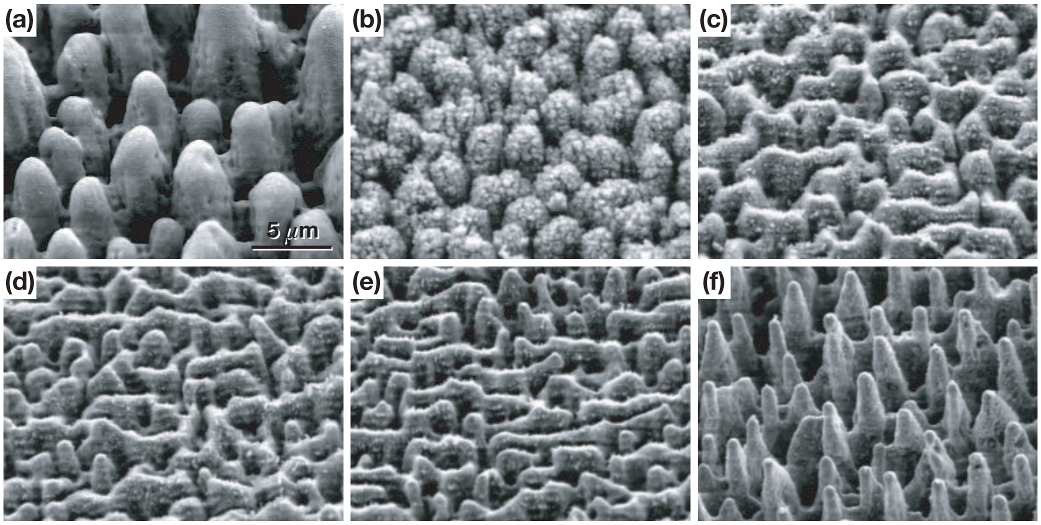

Figure 2.8: SEM images of the surface morphology for laser-textured silicon made at a fluence of 10 kJ/m^2 in different pressures of SF$_6$: (a) vacuum (10$^-$6 torr), (b) 5 torr, (c) 20 torr, (d) 100 torr, (e) 300 torr, and (f) 500 torr. Each SEM image is taken at a 45° angle to the surface with the same magnification, adapted from reference [52].

fs-laser irradiation in SF$_6$ (Figure 2.4). This is due to the incorporation of sulfur in the silicon lattice during laser-induced phase transition. Sulfur is a double donor that produces mid-gap impurity states between 100 meV to 300 meV below the conduction band of silicon [53]. These deep level states thus allow photons of smaller energy than the bandgap to excite electrons from the valence band to the defect states or from the defect states to the conduction band. The near unity sub-bandgap absorption is a result of both the geometric effect and the change in the electronic band structure of silicon. From the viewpoint of photovoltaic applications, these deep-level states provide stepping-stones for electrons to utilize sub-bandgap photons to transition from the valence band to the conduction band trough a two-step absorption process. This is promising for generating electrical power from the infrared range of the solar spectrum where 23% of the energy cannot be absorbed by crystalline silicon.

In fact, when irradiating silicon with fs-laser pulses, each melting and resolidification cycle occur on a timescale of nanosecond. The resolidifying solid/liquid interface moves at a speed of $\approx 10m/s$ as we will discuss in Chapter 4. The doping process thus occurs in a non-equilibrium manner where solute rejection is suppressed because the resolidification front progresses much faster than the diffusive velocity of sulfur ($\approx 1m/s$) [54, 55]. This gives rise to "hyperdoping", dopant incorporation at concentrations several orders of magnitude beyond the equilibrium thermodynamic solubility limit [41, 56]. At such a high concentration ($\approx 1at.\%$), the wavefunction of the dopant electrons is delocalized and an intermediate band forms via mechanism such as Mott insulator to metal transition [57, 58].

Luque *et al.* proposed the idea of intermediate band solar cell (IBSC) in which an intermediate band material is sandwiched between a typical p-n junction of a solar cell [59]. Including an intermediate band material into a traditional solar cell allows higher photocurrent generation via sub-bandgap absorption without sacrificing the open circuit voltage. Furthermore, lifetime recovery is predicted under the condition of insulator-to-metal transition. Overall, the theoretical efficiency limit of a single-junction IBSC under concentrated sunlight is 63%, much higher than the 40% Shockley-Queisser efficiency limit at the same operation condition [59–61]. Although there are still debates about whether or not lifetime recovery is present at high doping concentrations of deep level dopants, hyperdoping is a promising tool for fabricating intermediate band materials [62,63]. In Chapter 4 and 5, we will discuss the gas-phase (SF_6) doping mechanism and demonstrate how we can design the doping profile. We note that in parallel to the hyperdoping method using fs-laser, there are also other methods that can supersaturate silicon with deep level dopants, such as ion implantation and pulsed laser melting and plasma immersion ion implantation [64–67].

So far we have discussed both the surface texturing and hyperdoping using fs-laser. We emphasize that these two functions can be decoupled by a fine control of the laser parameters [68]. Texturing silicon with femtosecond-lasers has shown great contribution to enhance the absorption, short circuit current and the device efficiency in literatures [18, 69, 70]. Most of the work utilizes the benefit of surface texturing without hyperdoping. Nayak *et al.* reported a 14.2%-efficient crystalline silicon solar cell. They textured the silicon surface in SF_6 with fs-laser pulses then remove the laser-damaged layer before making a p-n junction. A spin-off company, SiOnyx, from our research group has applied laser texturing on 150-μm multicrystalline silicon wafers and reported an average efficiency of nearly 17% [71]. For hyperdoped silicon solar cell, Kontermann *et al.* holds the efficiency record of 4.5% [72].

2.3 Light-trapping for thin silicon solar cells

Commercial solar cells are typically made of 180-μm silicon wafers. These wafers are made by wire sawing from silicon ingots. Since the wires are on the order of 100 μm, each cutting produces almost the same volume of waste. This is the main factor for the high feedstock cost. Recently, researchers and manufacturers are focusing on using alternative kerfless methods to produce wafers thinner than 25-μm [73–76]. While there is an optimistic outlook in reducing the feedstock cost, another issue accompanying the reduction of material thickness emerges. Due to the weak infrared absorption coefficients of crystalline silicon, just a single light path is not sufficient for the material to absorb all the infrared light. Hence, photon management, making most use of the sunlight, becomes the key towards enhancing the device efficiency of thin crystalline silicon solar cells.

Fortunately, crystalline has a high refractive index ($n \approx 3.5$) that facilitates light-trapping, increasing the effective optical thickness of a material by total internal reflection that traps light inside the material to increase the total path length [77]. According to Yablonovitch's theory, a perfect Lambertian surface that scatters light in random directions creates a $4n^2$ enhancement in the effective optical thickness [78]. For crystalline silicon, perfect light-trapping translates to a 50 times increment in absorption. The effect of light-trapping is particularly important in thin film solar cells. Figure 2.9 demonstrates how crystalline silicon absorbs the sunlight at different materials thickness. We simulate assuming three scenarios: a) flat silicon, b) flat silicon with antireflection coatings, and c) silicon with both antireflection and Lambertian light-trapping surfaces. As the thickness decreases from 200-μm to 2-μm, the flat silicon is missing out more and more sunlight because light travels shorter and shorter distances in the material. Adding the antireflection coating improves the absorption across the whole spectrum for the 400-μm wafer. But it does not work well enough for thinner wafers. For industrially used and thinner wafers, the importance of light-trapping is obvious because just a single light path is not enough for crystalline silicon to absorb all the lower energy photons.

Researchers have been applying various surface structures to enhance light-trapping, such as: photonic crystals structures [79–81], plasmonic structures [82–85] or dielectric nanoparticles [86], nano-patterned and etched surface features [87, 88],

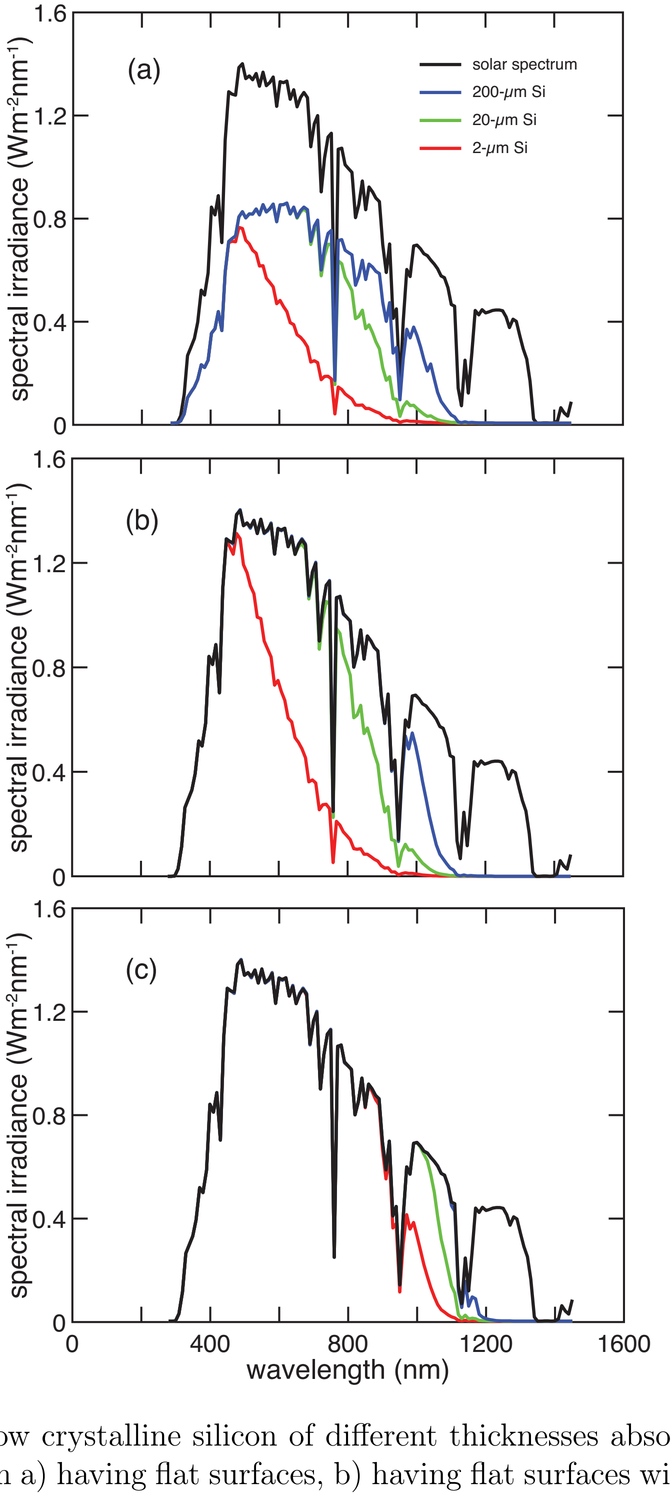

Figure 2.9: How crystalline silicon of different thicknesses absorbs the solar spectrum when a) having flat surfaces, b) having flat surfaces with antireflection coating, and c) having Lambertian surfaces with antireflection coating. The black curve in all figures is the solar spectrum (A.M. 1.5). The blue, green, and red curves represent the portion of solar spectrum that the material can absorb.

random textures [12,89]. In the following chapter, we discuss using laser-texturing to create efficient light-trapping surfaces for thin silicon solar cells.

Chapter 3

Femtosecond-laser texturing for light-trapping thin silicon solar cells

The trend of reducing materials cost of a solar cell by minimizing the active layer thickness urges extensive research in light management because a single light path no longer guarantees the material to absorption all the sunlight. One idea is to transform the flat material surface into randomized landscapes for light to scatter and be trapped inside the material due to total internal reflection. In this chapter, we demonstrate an enhanced photovoltaic efficiency in light-trapping thin silicon solar cells made by fs-laser texturing. This work is in collaboration with Benjamin Lee and Howard Branz at National Renewable Energy Laboratory.

3.1 Introduction

To compete with the mature wafer-based crystalline silicon photovoltaic technology that shares nearly 90% of the solar market, recent development in thin silicon photovoltaics aims for approaching high device efficiency and significantly reduction in the production cost. Furthermore, the stability of the module is another critical concern that motivates thin silicon technologies producing large-grained or single-crystal films including the porous silicon (PSI) process [90], thin wafer spalling [74], layer-transfer of thin silicon [73, 76], laser [91] and e-beam [92] recrystallization of silicon films, and seed and epitaxy approaches [89,93]. These technologies have great potential for scalability to large areas at low production cost. However, silicon has small absorption coefficients particularly for longer wavelength photons. It requires a material thickness of hundreds of microns or more to fully absorb all the red and near-infrared photons. Thus, a key challenge for silicon solar cells 50-μm or thinner is achieving high photocurrent by capturing more of the weakly absorbed sunlight than is possible in a single-pass through the silicon. To trap light in the material, obtaining longer effective path length of light without increase the physical thickness of the material, is therefore a crucial direction in the roadmap of achieving highly-efficient low-cost thin silicon solar cells.

As discussed in chapter 2, various methods have been employed to fabricate light-trapping surfaces [12, 80, 85–87]. In this chapter, we focus our discussion on a maskless random texturing method. There are several benefits of using random texturing methods. Ideally randomized surfaces give rise to Lambertian scattering, which is sufficient to attain the Yablonovitch light-trapping limit [78]. Furthermore, random texturing is likely to be industrially feasible because it does not require any pre-patterning steps. KOH etching is commonly used in the industry to texture (100)-oriented silicon wafers and the absorption of the textured surface is comparable to the Yablonovitch limit [12]. However, KOH etching typically removes many microns of silicon, which is not economical for thin silicon cells. Moreover, it does not work well with crystal orientations other than (100) or with multicrystalline silicon.

Two alternative methods to create randomized surface structures are texturing silicon with plasma etching [89] and laser pulses [18, 94]. Previous optical studies of laser-textured silicon primarily focused on the reduced reflectivity or the sub-bandgap absorption from concurrent hyperdoping with chalcogens during the texturing process [18, 94]. As described in Chapter 2, selecting a proper fabrication condition can decouple the texturing and the hyperdoping processes. In this chapter, we focus on purely texturing silicon with fs-laser pulses without introducing any chalcogen impurities. We investigate both the antireflection and light-trapping properties of the randomly textured silicon surfaces. We also make thin silicon solar cells to demonstrate the benefit of laser texturing for light-trapping.

3.2 Experimental

In this section, we describe experimental procedures to fabricate thin light-trapping silicon solar cells by fs-laser texturing. There are three main steps: 1) fabricate light-trapping surfaces using femtosecond laser pulses, 2) chemically etch the surface to remove laser-induced surface defects, and 3) device fabrication.

3.2.1 Laser texturing

We can create various surface textured with fs-laser pulses, depending on the laser parameters and the ambient gas environment [41]. We perform texturing in H_2 to passivate dangling bonds at the silicon surface. Texturing in H_2 also avoids large surface structures and material removal, as opposed to texturing in vacuum or SF_6. The surface morphologies of silicon textured in H_2 is similar to those textured in N_2, having blunt hills and valleys instead of sharp spikes. We can tune the size of the surface features by altering the laser fluence and the number of shots. In this work, we target wavelength-scale and larger surface features to: 1) reduce the reflectivity by directing reflected light to neighboring valley walls, and 2) scatter light at large angles, resulting in light-trapping with the assistance of total internal reflection inside the material.

We use a regeneratively amplified Ti:sapphire laser to perform surface texturing on four different silicon surfaces: 1) 2-μm polycrystalline silicon thin films grown by hotwire chemical vapor deposition, 2) 20-μm thin crystalline silicon wafers, 3) 50-μm crystalline silicon wafers, and 4) 400-μm crystalline silicon wafers. The laser pulses have a temporal duration of 100 fs, a center wavelength of 800 nm, and a repetition rate of 1000 Hz. Except for the 2-μm, all wafers are double side polished. We clean the surface of silicon with solvents (acetone, methanol, and isopropanol) before loading them into a chamber, which is pumped down to 10^{-5} torr before being back-filled with 100-torr of H_2. We use a scanning mirror system to raster scan the laser pulses on the silicon surface, achieving on average 100 laser shots per area at a fluence of 3 kJ/m^2. We illustrate the experimental setup in Figure 3.1.

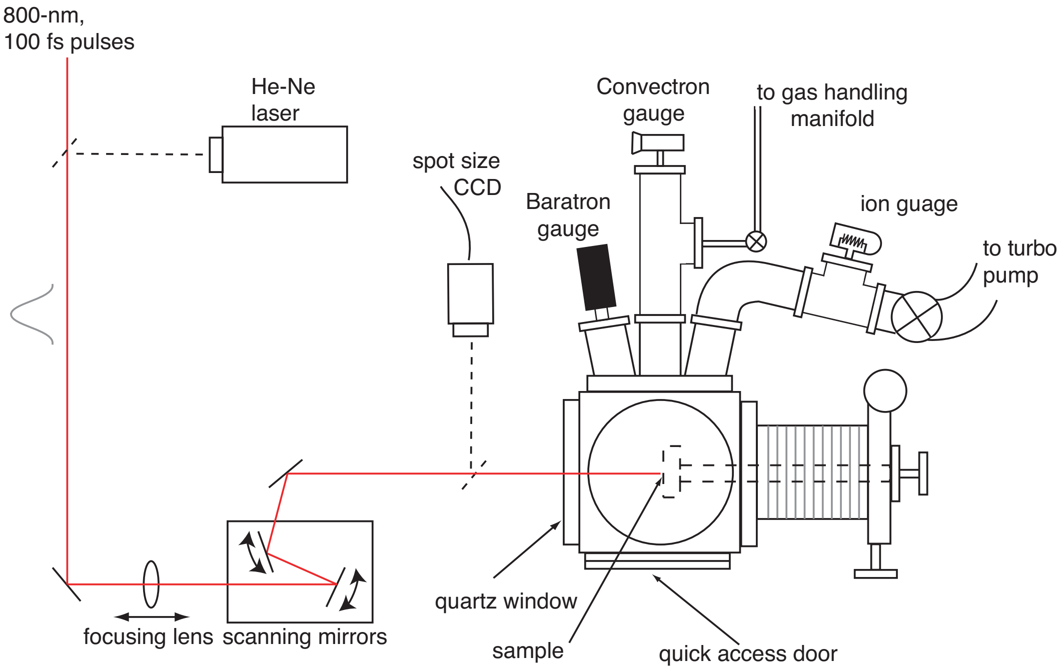

Figure 3.1: A schematic diagram of our fs-laser texturing apparatus. Two Galvo scanning mirrors direct and raster the fs-laser beam on the sample mounted in a chamber. A He-Ne laser is present for alignment purpose. A CCD camera is used to measure the spot size.

3.2.2 Chemical etching

Inevitably, laser texturing introduces polymorphs and extended defects to the silicon lattice. Therefore, we employ chemical etching to remove the unwanted laser damaged surface layer. First, we etch with KOH (40%) solution at 70 °C for 45 seconds. Then, we use a mixture of hydrofluoric acid : nitric acid : acetic acid (HNA etch) with a ratio of 2 : 5 : 15 for 3 minutes at room temperature. HNA is an isotropic wet etchant for silicon. The ratio of HNA determines the etch rate and the aspect ratio of the etched material. We chose this ratio to maintain the surface roughness made by laser texturing [13, 95, 96].

3.2.3 Device fabrication

We fabricate silicon heterojunction (SHJ) solar cells on a 50-μm crystalline silicon wafer to demonstrate the effect of light-trapping on the device performance. The float-zone wafer is phosphorus-doped (n-type) to a resistivity of 1-10 Ω·cm. Figure 3.2 illustrates the device structure. For directly comparing the performance of a textured cell and the flat reference cell, we perform laser texturing and chemical etching on half of the wafer as described in the previous sections and leave the other half unaltered. The wafer is then RCA-cleaned and HF-dipped to remove the native oxide immediately prior to deposition of the emitter. The emitter consists of 10-nm of p-type boron-doped amorphous silicon on top of 4-nm of intrinsic amorphous silicon made by plasma enhanced chemical vapor deposition (PECVD) onto the front (laser-textured) side. We deposit an 80-nm thick layer of indium tin oxide (ITO) as the front contact. On the rear side, 4-nm of intrinsic and then 10-nm of n-type phosphorus-doped amorphous silicon is deposited by PECVD. We form the back contact on the whole area of the wafer by depositing 80-nm of ITO followed by a reflective metal stack (1.5-nm Ti / 1-μm Ag / 100-nm Pd). On the front side, we deposit metal (50-nm Ti / 60-nm Pd / 1-μm Ag/ 100-nm Pd) and create patterns using photolithography. We isolate 0.05-cm^2 circular mesa cells by etching through the ITO and amorphous silicon layers in the area surrounding the cell. The front metal serves two functions: as a tiny contact pad on the cell mesa for the electrical measurement probe and separately covering the large area outside the cell mesa to block stray illumination.

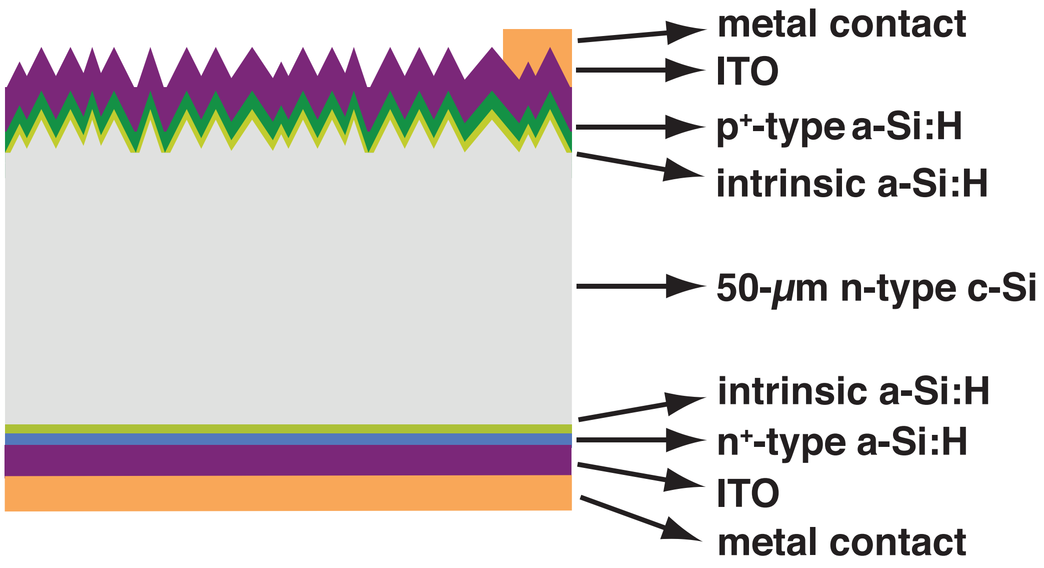

Figure 3.2: The architecture of our laser-textured thin silicon heterojunction solar cells.

3.2.4 Characterization

We examine the surface morphology and cross-section of the textured surface with a scanning electron microscope (SEM) and a tunneling electron microscope (TEM). We measure the optical transmission (T) and reflection (R) spectrum using a spectrophotometer equipped with an integrating sphere. Both the specular and diffusive light is collected. The absorption (A) is calculated by $A = 1 - T - R$. We perform external quantum efficiency (EQE) and current-voltage ($I - V$) measurements on both the textured and the flat cells under illumination of a solar simulator (A.M. 1.5).

3.3 Result

In Figure 3.3, we demonstrates the effect of laser texturing on the optical property and the surface morphology of a silicon thin film. The transparent 2-μm thin film turned from orange color to opaque after laser texturing. The SEM image shows that hills and valleys form randomly on the silicon surface after laser texturing. The size of these features is on the order of 1-μm. Additionally, we find some nanoscale features such as nano-pores and nano-particles on the textured surface.

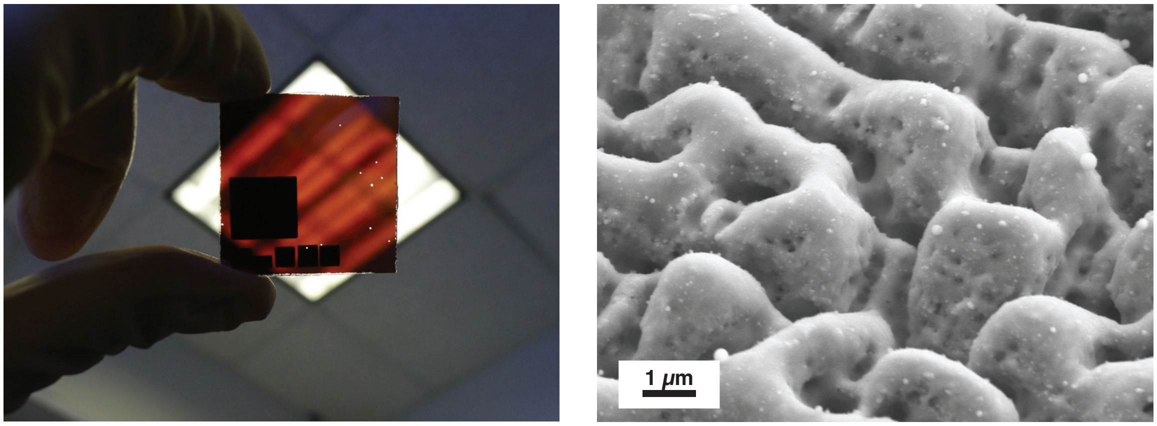

Figure 3.3: (Left) A 2-μm silicon thin film textured by fs-laser pulses. The structured regions appear to be black to the eye. (Right) An SEM image of the textured silicon surface from a 45° viewing angle. Hills and valleys having a size of about 1 μm form randomly on the silicon surface, which is suitable for antireflection and light-trapping.

We show the cross-sectional TEM image of one of the hills formed by laser pulses in Figure 3.4, revealing the crystallinity of the textured surface. We observe highly defected polycrystalline silicon and nano-voids instead of single crystalline lattices in the sub-surface area of the hill. The damaged region can be as deep as the height of the surface structures. We note that there is a layer of ITO covering the surface on top of an amorphous layer. They are both deposited onto the surface after laser texturing as the front contact for making a photovoltaic device.

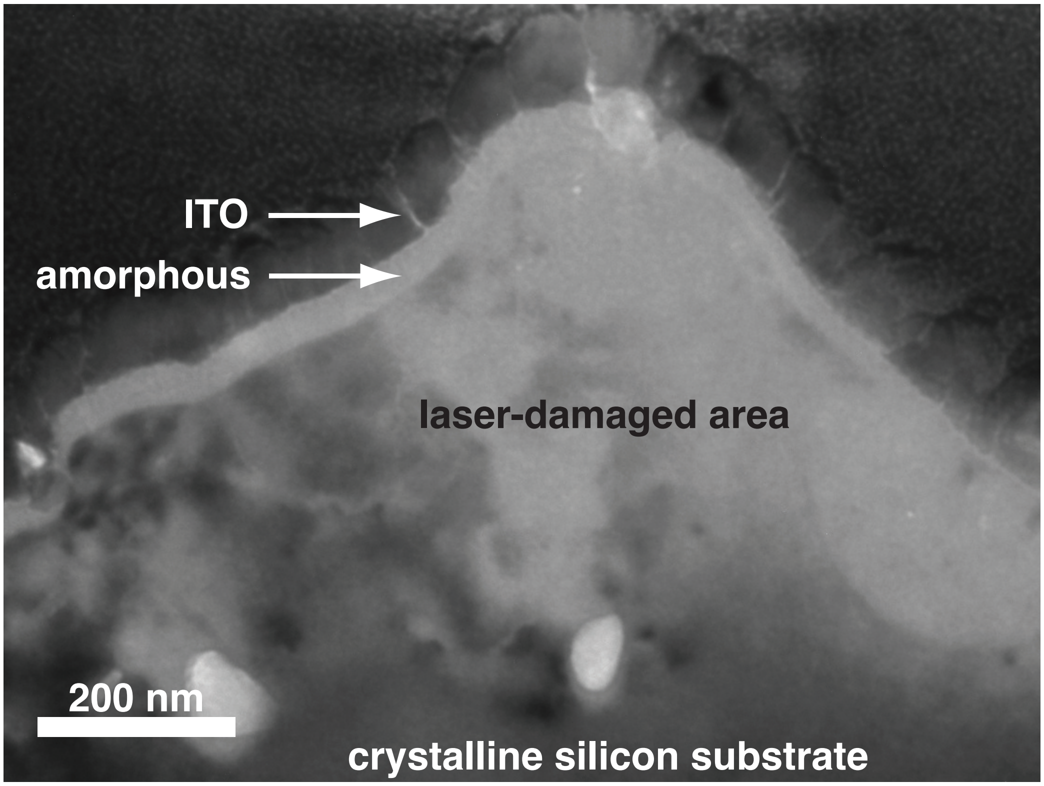

Figure 3.4: Cross-sectional TEM image of one of the hills on a textured silicon surface. The texturing process damages the crystallinity and results in lattice defects and voids inside the sub-surface region. We note that a layer of ITO and amorphous silicon is deposited onto the surface for fabricating a device.

In Figure 3.5, we compare the surface morphologies of two samples, with one as-textured (Figure 3.5 (Left)) and the other textured and etched (Figure 3.5 (Right)). Before etching, we observe nano-indentations and voids at the surface. The etched sample is slightly smoother and has shallower surface features than its as-textured counterpart. However, it is free of nano-indentations and nanoparticles.

We investigate the optical properties of our laser-modified silicon surfaces by comparing the laser-textured wafers to their flat references. We also report the effect

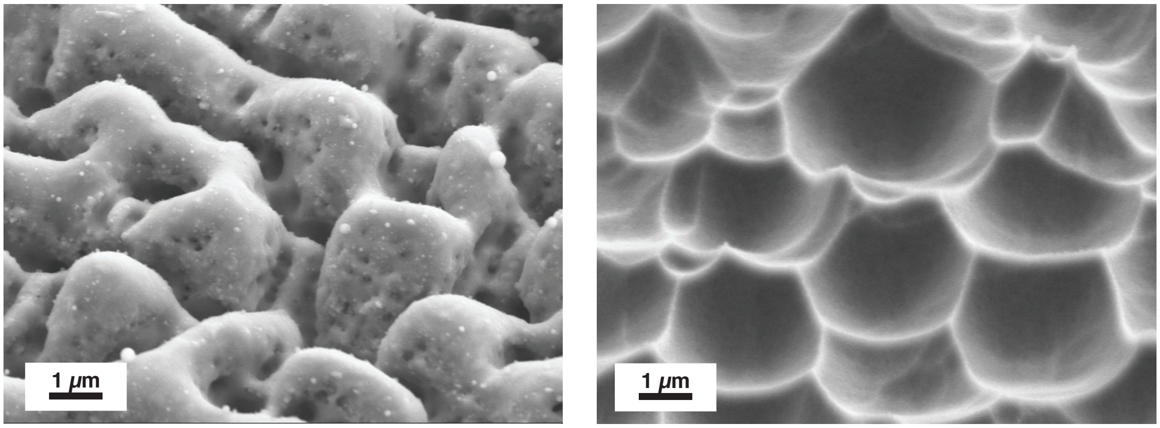

Figure 3.5: (Left) SEM image of the as-textured surface from a 45° viewing angle. (Right) SEM image of the same sample after wet etching to remove the laser damaged surface layer.

of the additional chemical etching on the optical properties. To elucidate the antireflection and light-trapping properties, we study the reflectivity and absorption for textured wafers that are 400-μm and 20-μm thick. We include the simulated absorption for both the 400-μm and 20-μm wafers under two conditions: 1) a flat surface with an optimized antireflection coating on top (75 nm of silicon nitride with a reflective index of 2), and 2) a Lambertian surface without the antireflection coating. We first examine the 400-μm wafers. In Figure 3.6 (a), we observe that the reflectivity of both the modified wafers is lower than the flat wafer across the entire visible spectrum. The reflectivity of the as-textured wafer is the lowest. After wet etching, the reflectivity is between the flat wafer and the as-textured wafer. Figure 3.6 (b) shows the same effect of reflectivity reduction in the 20-μm wafer that has been textured and etched. Figure 3.6 (c) and (d) compares the absorption spectrum of the modified silicon wafers to the flat wafer and the theoretical simulations. For samples that have been textured and etched, the 400-μm and 20-μm wafers have qualitatively similar absorption. The absorption is enhanced across the visible spectrum up to silicon's bandgap compared to the flat wafers. The surface-modified wafers exhibit a lower absorption than the wafer with optimized antireflection below 1000 nm and 800 nm for the 400-μm and 20-μm wafers, respectively. However, the absorption enhancement almost approaches the Yablonovitch (Lambertian) limit beyond 1000 nm and 800 nm for the 400-μm and 20-μm wafers, respectively. We note that the as-textured wafer has a higher absorption than the textured and etched wafer across the entire spectrum. Particularly, significant sub-bandgap absorption in the as-textured wafer is reduced to about 5% after the wet etching.

Figure 3.7 demonstrates the angle-dependent absorption spectrum of a 20-μm silicon wafer that has been textured and etched. The angle is defined by the difference between the incident direction of light and the surface normal, with zero degree corresponding to normal incidence. A larger angle means that the sample surface normal is tilted farther away from the incident light path. While the absorption in the visible range decreases slightly with increasing incident angles, it remains unchanged for near the bandgap spectrum.

In Figure 3.8, we present the performance of our light-trapping devices. We label our laser-textured and wet-etched devices as the "textured" device. First we examine the photon to electron conversion efficiency at visible and near IR spectrum. We define the external quantum efficiency (EQE) as the number of the photo-generated electrons at zero bias voltage divided by the number of the incoming photons. The EQE of the textured device is higher than the flat device across the entire spectrum (Figure 3.8 (Top)). The EQE ratio of the textured device to the flat device is between

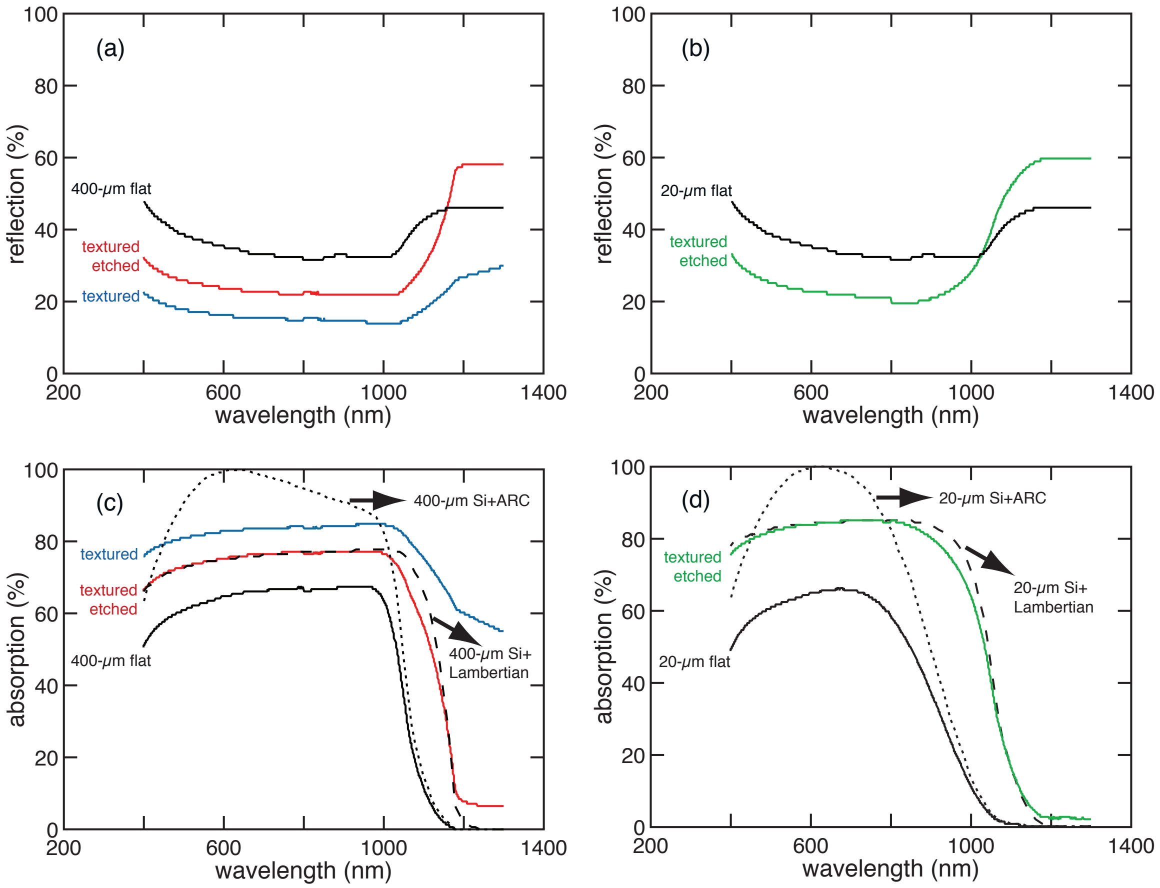

Figure 3.6: Optical properties of 400-μm and 20-μm silicon wafers that are either treated with only laser texturing or with additional wet etching, as labeled in the figures. Optical properties of the flat wafers are included as reference. (a) and (b) show the reflectivity of the 400-μm and 20-μm wafers, respectively. (c) and (d) show absorption of the 400-μm and 20-μm wafers, respectively. Data collected from the flat samples are included for reference. Theoretical simulations are presented in (c) and (d) for comparison. The dotted lines represent the simulated absorption of a silicon wafer with antireflection coating (ARC) of an optimized thickness of 75 nm. The dashed line represents the simulated absorption of a silicon wafer with a Lambertian light-trapping surface.

1 and 2 in the visible spectrum (Figure 3.8 (Bottom)). However, it increases from 1.5 to 5 when the wavelength, λ, increases from 900 nm to 1100 nm. Figure 3.9 shows the current-voltage ($I-V$) curves of both the textured and the reference cells. The short

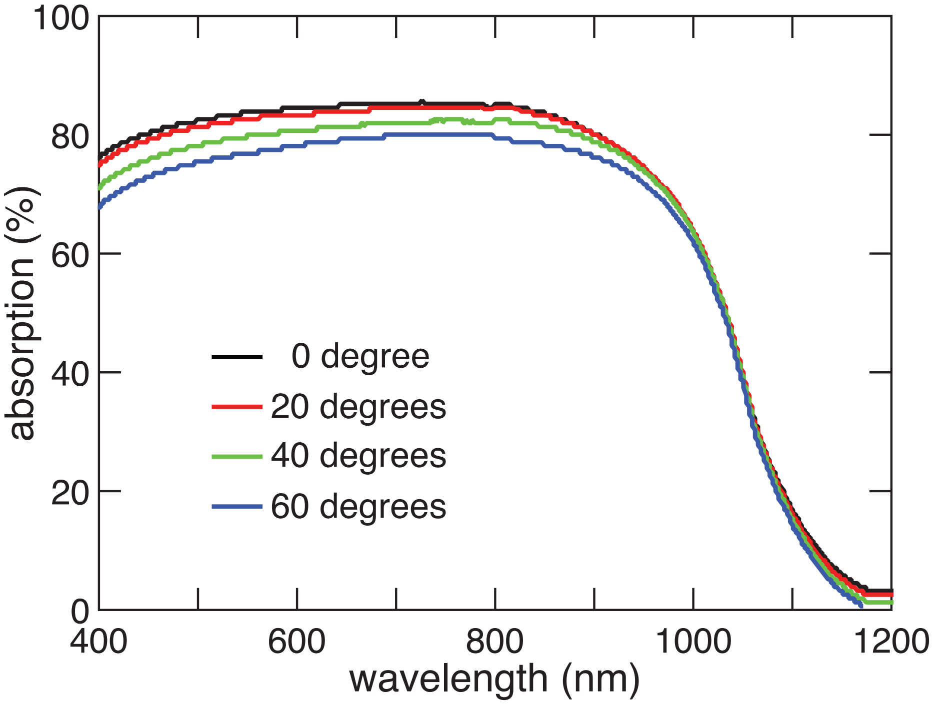

Figure 3.7: Absorption of a 20-μm silicon wafer that has been textured and etched as a function of incident angle. The incident angle is relative to the surface normal. The absorption in the near bandgap spectral range is nearly identical for all angles.

circuit current, defined as the current at zero bias voltage, of the textured device is $\approx 15\%$ higher than the flat device. The open circuit voltage, defined as the voltage at zero current condition, is the same for both devices. Table 3.1 lists the values of open circuit voltage, short circuit current, fill factor, and efficiency for both the textured and the flat reference device.

3.4 Discussion

To obtain efficient antireflection and light-trapping, we aim to create wavelength-size and larger features on the silicon surface. We select a fluence (3kJ/m^2) that is just above the ablation threshold, which is high enough to modify the surface morphology while avoiding significant ablation [97]. Thus, the change in surface morphology is accompanied by a negligible amount of material loss. During the texturing process, each fs-laser pulse locally melts silicon at the surface to a depth of approximately 50 nm. Meanwhile, molten capillary waves form as a result of an inhomogeneous energy deposition from interference of the incoming laser pulse and scattered light at the surface. Within a short melt duration, on the order of nanoseconds, the surface waves are frozen in space to form ripples before they could dissipate away [45, 49, 50, 98, 99]. Successive laser irradiations cause these surface ripples to grow into small hills and valleys. The hills and valleys have a spacing of about 1-2 μm, which is perfect for photons of about 1 μm and smaller wavelengths to reflect multiple times between these structures and enter the material in random directions. We can clearly observe this effect in Figure 3.3 (Left). While the 2-μm silicon thin film is transparent to the red photons, the textured area no longer allows the red photons to transmit through and appears to be black.

Unfortunately, laser texturing also results in structural defects in the silicon lattice as seen in the cross-sectional TEM (Figure 3.4) and nanoscale pores and indentations on the surface structures as shown in Figure 3.3 (Right). Previously, we studied the microstructure of the surface textures by TEM and Raman analysis. Our investigation suggested that fs-laser induced fast melting and resolidification on a textured surface generates stresses, which deform the silicon lattice and result in the formation of polymorphs and extended defects. The plastic deformation could occur in regions as deep as 1 μm below the surface [100]. Although the polymorphs can be annealed out at low temperatures, the extended defects cannot be easily removed. Previously, we have tried to anneal the laser-textured silicon in an oven at 600°C to recover the lattice structure. The silicon polymorphs and amorphous phases disappear after annealing under Raman analysis. We also performed absorption measurements that show a reduction in the sub-bandgap absorption mediated by the structural defects. However, the device shows an enhancement in EQE only in the near bandgap spectrum; the overall conversion efficiency is poor [101].Our failure on demonstrating an enhanced photocurrent in a textured and oven-annealed silicon thin film solar cell implies that recovering the laser-damaged lattice is not trivial. The extended defects cannot be removed within a reasonable annealing temperature and time duration. Furthermore, the presence of nano-indentations at the surface prevents a good passivation since the amorphous layer thickness is only a few nanometers. Incomplete surface coverage of the amorphous layer results in poor junction quality, as reflected in the low shunt resistance and a small V_{oc} [101]. We thus conclude that it is mandatory to remove the damaged surface layer.

Wet etching is an economical way to achieve this goal. We choose a two-step etching recipe to remove the surface layer while preserving the randomized surface features created by laser texturing. The etched surface is smoother than the as-textured surface and free of obvious morphological defects (Figure 3.5). We note that just the etching process itself will not produce the same textures on a flat silicon surface. More importantly, the entire process, including laser texturing and wet etching, only removes 1- 2 μm of material. Therefore, our approach is more compatible with thin film silicon solar cells than the conventional KOH etching technique that removes many microns of silicon.

Next we discuss the optical properties of the textured silicon wafers with different thicknesses (400-μm and 20-μm). Figure 3.6 (a) shows the reflectivity of the 400-μm wafers with different surface treatments. The as-textured sample has the largest roughness in morphology and therefore the lowest reflectivity. Wet etching increases the reflectivity slightly because the surface features become shallower and smoother. In Figure 3.6 (b), we also observe similar reduction in the reflectivity comparing the textured and etched 20-μm wafer to the reference. We see an increase in the absorption corresponding to the decrease in reflection for both of the roughened 400-μm and 20-μm wafers (Figure 3.6 (c) and (d)). As shown in the simulated absorption curves, antireflection benefits the absorption below 1000 nm and 800 nm for the 400-μm and 20-μm wafer, respectively. For longer wavelengths, light-trapping plays an important role in the enhanced absorption for all the roughened samples. We note that the significant sub-bandgap absorption in the as-textured samples is due to structural defects created by the laser process. After wet etching, the sub-bandgap absorption decreases to about 5%. The residual sub-bandgap absorption is similar to that of a wafer etched by KOH. Therefore, we conclude that the etching process has removed most of the laser induced structural defects. For both the 400-μm and 20-μm wafers, the laser-textured and etched samples absorb like a Lambertian light-trapping material, which we attribute to the nearly ideal random textures created by our fs-laser process. This is supported by angle-dependent absorption measurements of a 20-μm wafer that has been laser-textured and etched (Figure 3.7). The absorption at wavelengths near the bandgap is independent of the incident angle. An ideal Lambertian surface produces completely randomized light scattering, regardless of the incidence angle of illumination. Therefore, the fact that the absorption for the near bandgap photons is independent of the incident angle of light provides strong evidence that we have created a Lambertian surface. Comparing the enhanced near bandgap absorption in the 400-μm and 20-μm wafers, we clearly see the importance of light-trapping when reducing the wafer thickness. Although our textured surfaces does not absorb perfectly in the visible spectrum as the silicon with optimized antireflection coating, we could utilize the excellent light-trapping properties created by random texturing and add an extra layer of antireflection coating to capture reflection loss. We apply this method to our silicon heterojunction solar cells.

We have successfully demonstrated the enhanced performance in a 50-μm solar cell made of laser-textured and etched silicon. The device efficiency increases from 10.2% to 11.6%, a nearly 15% increment, due to an increase in the short circuit current J_{sc} from 26.5 to 30.0 mA/cm^2. The improvement in the photocurrent does not sacrifice the open circuit voltage. However, we emphasize that the value of V_{oc} (500 mV) is smaller than a good heterojunction silicon solar cells ($>$ 700 mV) [102]. In fact, the wafer itself has a low carrier recombination lifetime of 6 μs evaluated by the quasi-steady-state photoconductance lifetime measurements.

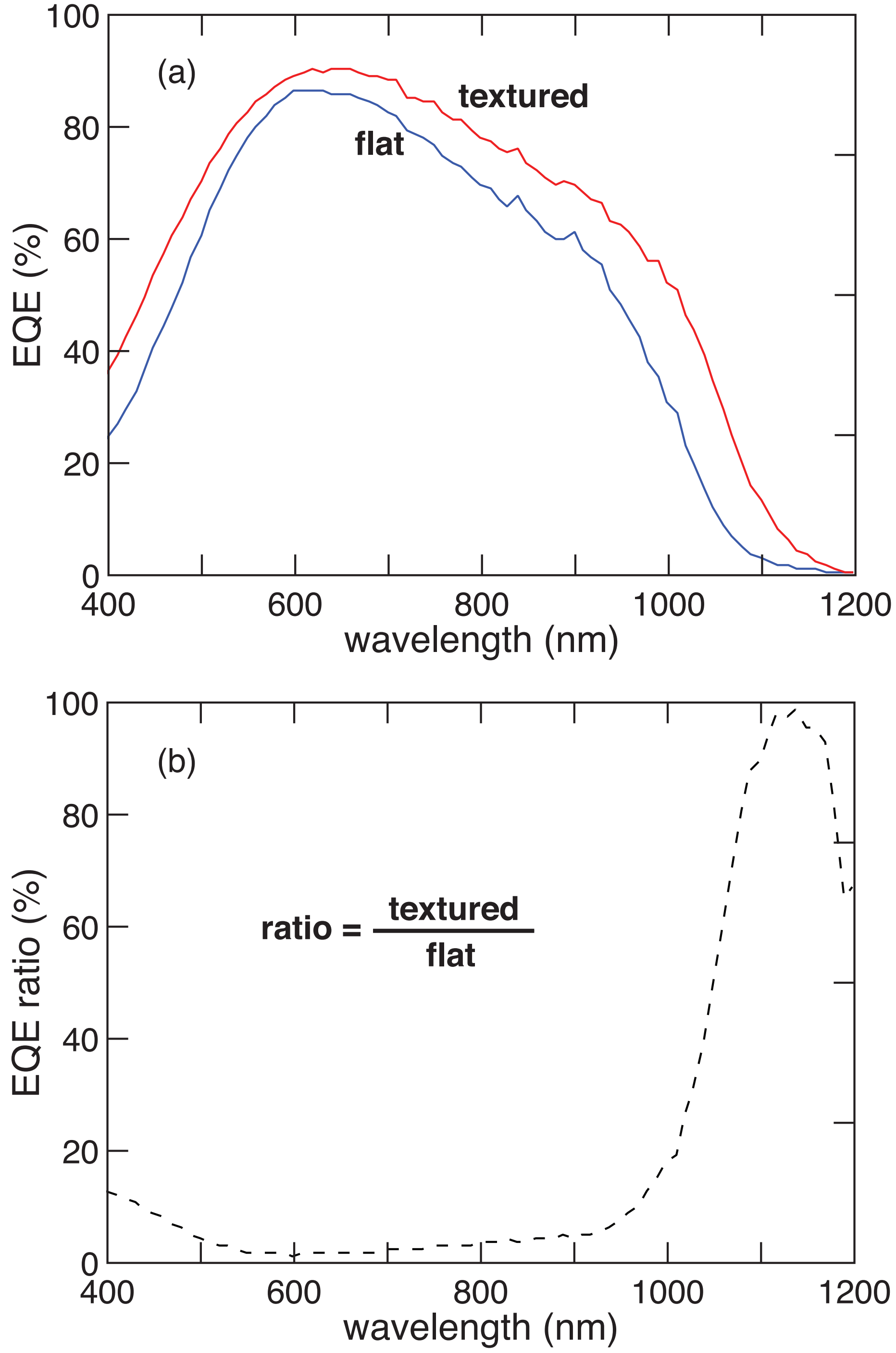

Figure 3.8: (Top) Comparison of the EQE of a laser-textured and etched cell, labeled as "textured", (red) and a flat cell (blue). (Bottom) The EQE ratio of the textured cell to the flat cell. The EQE enhancement in the near bandgap spectrum is significantly higher than the visible spectrum.

Typically, a high quality wafer should have a lifetime of 1 ms or larger. We attribute the small V_{oc} to the poor wafer quality. We therefore cannot comment on whether or not the laser or chemical process has effect on the junction quality because the bulk material quality has a significant effect on the value V_{oc}, making it insensitive to the junction quality. However, from the surface morphology shown in Figure reffig:etch, we expect a good passivation during the amorphous layer deposition which should give rise to the formation of a perfect junction.

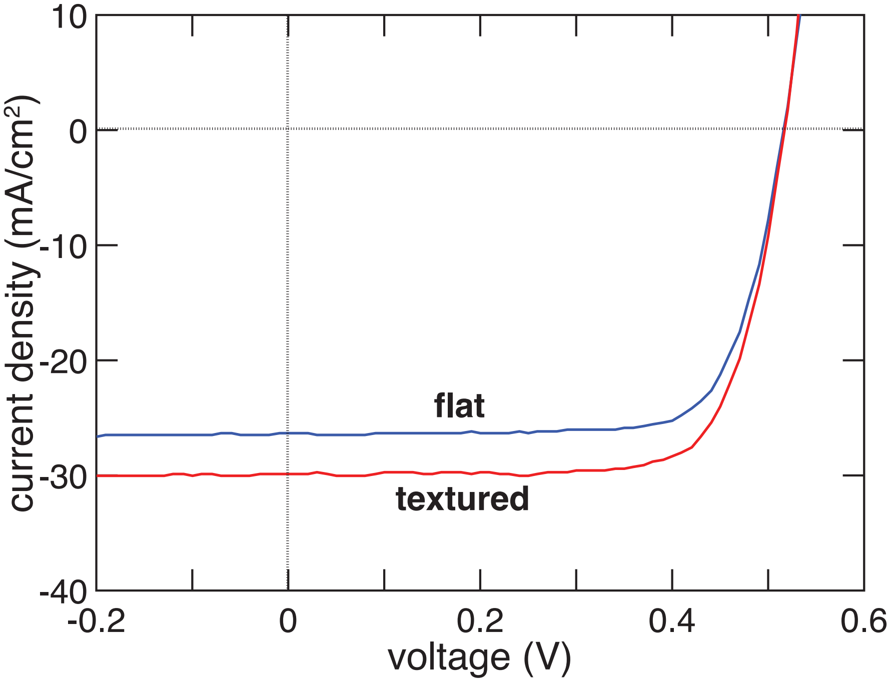

Figure 3.9: The I-V curves of the same set of devices. The textured cell has nearly the same open circuit voltage as the flat cell but a ≈ 15% enhancement in the short circuit current.

Examining the EQE assures our success in producing the Lambertian light-trapping surfaces and the benefit of it to the overall energy conversion efficiency. The laser-textured cell has improved EQE across the entire spectrum compared to the flat

Table 3.1: Short circuit current (J_{sc}), open circuit voltage (V_{oc}), fill factor, and efficiency of the textured and etched cell and the flat reference cell.

Sample	J_{sc} (mA/cm^2)	V_{oc} (mA/cm^2)	Fill factor (%)	Efficiency (%)
Flat	26.5	516	74.7	10.2
Textured and etched	30.0	517	74.5	11.6

reference cell (Figure 3.8), consistent with the enhanced absorption discussed in the previous paragraph. For $\lambda < 900$ nm, silicon has absorption lengths larger than the thickness of the wafer (50 μm), meaning all the light entering the material should be absorbed within a single-pass through the material. Therefore, we can attribute the enhancement in EQE to the reduced reflection for $\lambda < 900$ nm. For $\lambda > 900$ nm, the EQE enhancement cannot be simply due to antireflection because the material is not thick enough to capture all the light if it were to pass through only once. However, we observe an EQE improvement of a factor between 2 to 5 for $\lambda > 1000$ nm, far too large to be explained by the small change in antireflection alone. We attribute this enhancement to the effect of light-trapping on the weakly absorbed red-photons.

3.5 Conclusion

Our fs-laser processing technique allows us to create randomly-textured surfaces on silicon that leads to antireflection and light-trapping. Although the anti-reflection properties can be further improved, the light-trapping properties of our textured surfaces approach the Yablonovitch limit for Lambertian surfaces. However, the as-textured surfaces contain undesirable nano-indentations and sub-surface structural defects to a depth of nearly 1 μm. We can easily remove the damaged layer with a wet etching recipe that maintains the random roughness created by the laser treatment and the excellent angle-independent light-trapping property.

We fabricate heterojunction solar cells on 50-μm thick, laser-textured and etched silicon wafers to demonstrate the benefit of light-trapping on thin silicon solar cells. The EQE of a textured cell is improved significantly at the near bandgap range of silicon's absorption spectrum. Compared to the flat reference cell, the textured cell has a nearly 15% improvement in the short circuit current and the energy conversion efficiency. We believe that laser texturing is a promising technique for fabricating thin film light-trapping solar cells for many reasons. First, laser processing has been employed in the solar industry for large-area, high-throughput fabrication. Second, this technique applies to various material systems regardless of the crystal orientation and crystallinity. Third, this process is mask-less and does not require multiple-step patterning. We encourage further engineering of the fabrication process to obtain high quality textured surface that eliminates the need of chemical etching. For example, it might be possible to design a pulse sequence that produces surface textures while preserving the crystallinity.

Chapter 4

Mechanism of femtosecond-laser hyperdoping

In this chapter, we study fs-laser hyperdoping for intermediate band photovoltaic applications. Irradiating silicon with fs-laser pulses in the presence of dopant precursors allows incorporation of non-equilibrium concentrations of dopants that leads to intermediate band formation. For useful applications, the ability to control the doping concentration, distribution, and the position and width of the intermediate band in the electronic bandgap are crucial. Understanding the hyperdoping mechanism is thus the key to further manipulation of our doping technique. In this chapter, we focus on elucidating the physical processes underlying fs-laser hyperdoping using a gas phase species, SF_6, as the dopant precursor. We apply an *in situ* pump-probe technique to monitor the melting and resolidification dynamics and provide constraints on the theoretical modeling of the hyperdoping process.

4.1 Introduction

Introducing deep level dopants in semiconductors leads to sub-bandgap absorption via a two-step absorption process that promotes the valance band electrons to the conduction band [103]. While sub-bandgap absorption allows a semiconductor to capture more energy from the sunlight, extracting the extra photo-excited carriers out from the material before they relax back to the valence band is not trivial. The presence of deep level impurity states mediates non-radiative recombination, causing a reduction in the carrier lifetime [104,105]. Therefore, efforts in developing impurity photolvoltaics back in the 60s did not show any promise [106]. Recently, Luque and Marti proposed the idea of intermediate band photolvoltaics — introducing a band of delocalized impurity states to utilize the enhanced sub-bandgap absorption while suppressing the recombination rate [59]. It is predicted that an optimized intermediate solar cell could break the Shockley-Queisser efficiency limit for single-gap materials [60]. Approaches toward creating intermediate band materials includes quantum dots methods and bulk methods [107]; we focus on the latter in this thesis. By highly doping of deep level impurities above the insulator-to-metal transition limit, it is expected that delocalization of the dopant electron wavefunctions will allow lifetime recovery [108]. Researchers have provided evidence of lifetime recovery in silicon highly doped with Titanium [63].

The chalcogen, including S, Se, and Te, is another candidate system for producing an intermediate band in silicon. It is recently reported that insulator-to-metal transition occurs in silicon supersaturated with sulfur [64]. Although there is debate about whether or not lifetime recovery should occur under insulator-to-metal transition, it has been shown that the cross-section for recombination through sulfur impurities in silicon can be significantly reduced relative to isolated impurities cite at high doping concentrations below the Mott-transition limit [62, 109]. The Mazur group has been developing a laser technique that allows incorporation of dopants beyond the equilibrium solubility limit — a requirement for producing chalcogen-doped silicon with insulator-to-metal transition and reduced carrier recombination rate. By irradiating fs-laser pulses on silicon in the presence of gas phase or thin film precursors, silicon can be doped with ≈ 1 at.% of chalcogens [110]. Incorporation of calcogens allows sub-bandgap absorption up to 5-10 μm [111]. Furthermore, It has been shown that sulfur-hyperdoped silicon by fs-laser has sub-bandgap responses in photodiodes [112].

Besides laser hyperdoping, supersaturating materials with doping concentrations beyond the equilibrium solubility limit have also been achieved by a combination of ion implantation and pulsed laser melting over decades ago. Here researchers have carried out extensive studies on the mechanism leading to supersaturation. Aziz *et al.* performed a series of studies to understand the solid-liquid interface kinetics and its relation to the origin of the nonequilibrium dopant incorporation [113–117]. In Aziz's model, pulsed-laser-induced rapid solidification facilitates solute trapping, i.e., the suppressed rejection of solute from the supersaturated solid phase to the liquid phase at the solid-liquid interface. The velocity of the solidifying melt front and the level of solute trapping has a nonlinear relationship [117]. When the solidification velocity is much larger than the diffusive velocity, dopants in the freshly solidified phase cannot jump across the interface before the solidification front proceeds away from them.

With a thorough understanding of the interface kinetics and the classical heat and solute transport mechanism, Aziz's model precisely predicts the doping profile after pulsed laser melting. We note that this process is typically done with lasers having tens-of-nanoseconds pulse durations instead of fs-lasers [65, 118].

While knowledge on the nanosecond-laser-induced supersaturating sheds light on possible fs-laser doping mechanism, a priori it is unclear to which extent the two mechanisms can be comparable. Hyperdoping with Ti:sapphire fs-laser (800 nm, 100 fs) induces different phase transition processes compared to the typical pulsed-laser melting with ns-lasers. This is because nonlinear absorption dominates over linear absorption in the regime of fs-laser hyperdoping [119]. In the linear regime, electronic excitation from the valence band to the conduction band is achieved by absorbing photons of energy larger than the band gap. When the incoming photons are squeezed in space and time such as in an ultrafast laser pulse, multi-photon absorption takes place. In this scenario, the valence electrons can be promoted to the conduction band by consecutive absorption of photons having energy smaller than the bandgap. We can write the total absorption coefficient as $(\alpha+\beta I)$, where α is the linear absorption coefficient, I is the laser intensity, and β is the nonlinear absorption coefficient. The level of nonlinear absorption, βI, is one order of magnitude larger than the linear absorption, α, at a typical doping fluence of 4 $\mathrm{kJ/m^2}$ using a Ti:sapphire laser of 100-fs pulse duration [119]. Photo-induced carrier concentrations can be as high as 10% of the total valence electrons in silicon with fs-laser excitations [120]. Under this highly nonequilibrium condition, the material could experience surface plasma generation, nonthermal melting, and suppressed electron-phonon scattering [121–123]. Due to the extremely different condition as opposed to the ns-laser irradiation, we need closer examinations to elucidate to what extent the fs-laser hyperdoping follows the same physical mechanisms as the ns-laser treatment.

Previously, Winkler's work on hyperdoping silicon with varying fluences suggested melting is an essential step for hyperdoping [58]. Despite missing experimental evidence of the thermal history and the transport processes, Mangan *et al.* adopted Aziz's model to describe the fs-laser doping process based on classical heat and solute diffusion and solute trapping [124]. In the adopted model, fs-laser pulses excite the material instantaneously upon the absorption of photons following the Beer-Lambert law. The initial temperature profile is set to be the same as the initial distribution of photo-excited carriers. These assumptions are based on two facts. First of all, the laser pulse duration (100 femtoseconds) is much shorter than the time scale for electron-phonon scattering (hundreds of femtoseconds). Secondly, thermal diffusion occurs on a time scale (tens to hundreds of picoseconds) much longer than the time it takes for the electron and phonon systems to reach equilibrium (a few picoseconds) [122]. With the initial temperature distribution surpassing the melting temperature, the model assumes that the material melts heterogeneously from the surface proceeding into the bulk. As heat dissipates into the bulk, the solid-liquid interfacial temperature falls below the equilibrium melting temperature so that it becomes energetically favorable for the interface to turn around and start resolidifying. Dopants, in the form of SF_6, enter and transport diffusively in the melt during the time period when the materials is molten. Additional to the classical picture used for heat and solute diffusion, the model adopts the physics of solute trapping developed in Aziz's model [113].

Although the numerical model contains various material parameters of which several have not been determined independently, it reproduces experimentally measured concentration profiles with varying parameters in a reasonable regime [124]. This suggests that fs-laser hyperdoping may indeed follows the classical transport processes coupled to the non-equilibrium phase transition at the solid-liquid interface. However, different sets of parameters could produce the same profiles due to a lack of knowledge on how long the materials stays molten and how fast the molten phase resolidifies. Thus, we need direct experimental investigations to clarify whether the discussed processes cause the hyperdoping and provide constraints on the unknown parameters for the numerical model to reproduce the actual processes. Specifically, we could constrain the nonlinear absorption coefficient and the effective fluence if the time-dependent position of the solid-liquid interface is no longer unknown. Thus, it is crucial to perform independent experiments to provide information about the melt dynamics.

In this chapter, we answer these previously unknown questions: 1) what is the melt dynamics, and 2) how do we control the melt dynamics? We apply a pump-probe method to observe the optically induced change in the surface reflectivity during fs-laser hyperdoping and extract the solid-liquid interface position using a multilayer model. Direct measurements of the resolidification velocity and melt duration allow us to determine parameters and engineer the hyperdoping profile with the validated simulation tool.

4.2 Experimental

4.2.1 Pump-probe reflectivity measurements

We present the schematic illustration of our experimental setup in Figure 4.1. We build a pump-probe spectroscopy on top of the existing fs-laser doping apparatus to monitor the change in the sample surface reflectivity during the doping process. A regeneratively amplified Ti:saphhire laser produces pulses of 100 fs duration at center wavelength of 800 nm. The laser pulse is split into a pump pulse and a probe pulse at the beamsplitter. The pump pulse is directed to the sample via a motorized delay stage that has a precision of 3 μm, which translates to a 10-fs time resolution. The delay stage is able to separate the pump and the probe by up to 600 ps. For longer delay time, we extend the probe arm to match the corresponding distance for delay time between 1 to 6 ns. We pass the probe pulse through a half waveplate and a polarizing beamsplitter to change the polarization from horizontal to vertical. The probe pulse then travels through an optical parametric amplifier (OPA) that outputs fs pulses of tunable wavelengths. The probe pulse is centered at 800 nm for the experimental results presented in this thesis. We focus the pump and the probe pulses to about 1000 μm and 150 μm in diameter at FWHM, respectively, on the silicon surface. The intensity of the probe is attenuated to 6 orders of magnitude smaller than the pump for minimizing perturbation to the experiment. A polarizer is used to filter out the scattered pump pulses so that the detector is only collecting the vertically polarized (S-polarized) probe pulses.

One crucial step in a pump-probe experiment is to define the zero point in time,

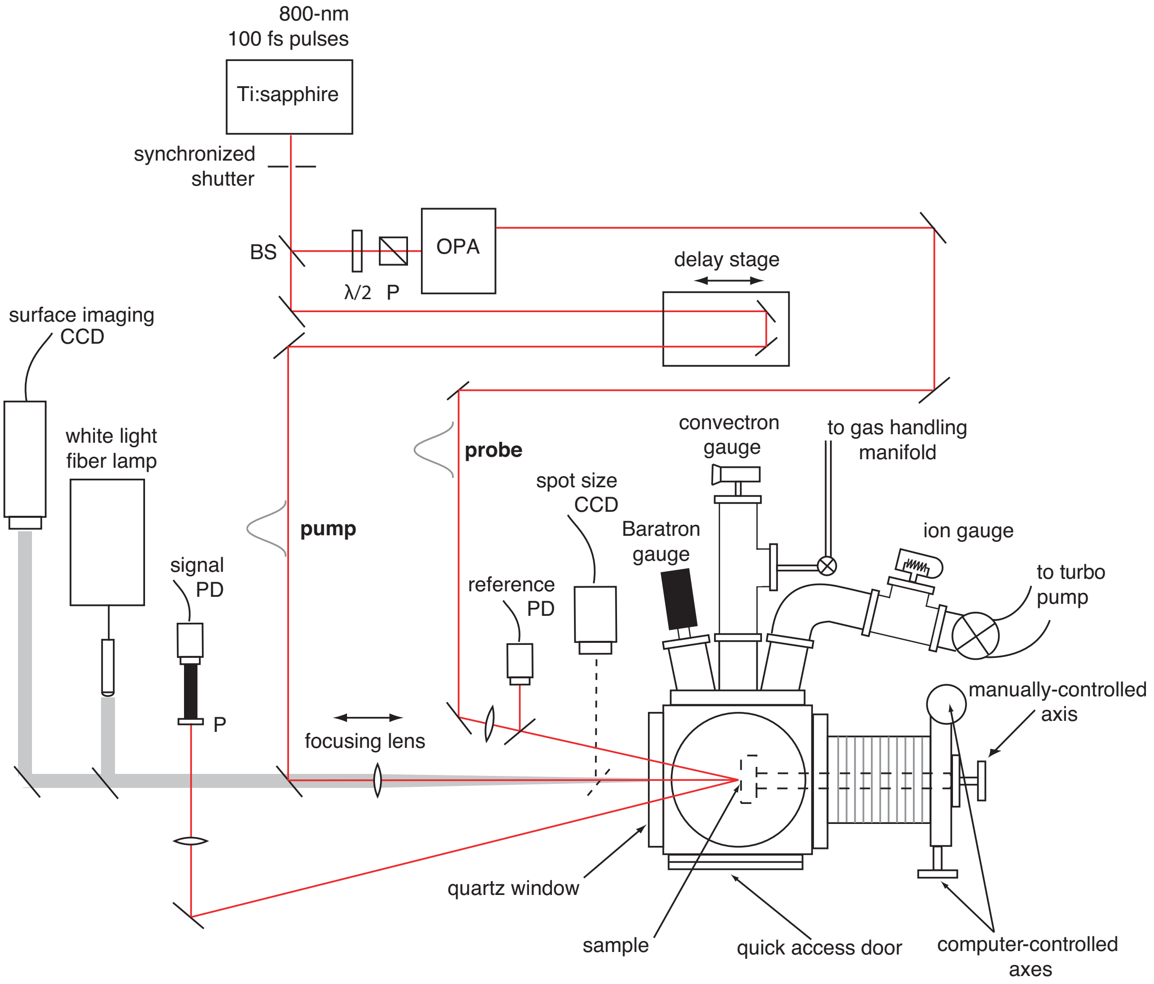

Figure 4.1: Schematics of our hyperdoping and pump-probe apparatus. P=polarizer; BS=beam splitter; $\lambda/2$=half waveplate; PD=photodiode.

when the pump and the probe pulses have traveled the same distance before arriving at the sample surface. We first overlap the pump and the probe on the surface of a BBO crystal that is placed in front of the chamber. We optimize the laser power so that the second harmonic light generates only when the pump and the probe overlap in time and space. The BBO crystal assists us to identify approximately where the time zero is and make sure the delay stage is well positioned. For actual measurements, we use a small fluence (≈ 0.5 kJ/m^2) to pump the silicon wafer and cause optically induced changes in the surface reflectivity. We maximize the change in the detector signal by overlapping the two pulses in time and space. This process does not introduce any damages to the irradiated area because we are only exciting a small portion of electrons that eventually heat up the lattice to a negligible degree.

We use a mechanical shutter to select single pulses out of a 100-Hz pulse train. The shutter is synchronized with the signal processing system, where an oscilloscope collects signal from both the reference and the signal detectors. The reason for having two detectors is to minimize the noise coming from the 10% variation in pulse energy from shot to shot. Considering useful applications, it requires multiple laser irradiations to manipulate the doping profile. Therefore, we perform measurements on the same area for multiple times to understand how the melt dynamics evolves over laser irradiations. Since the laser fluence chosen is above the damage threshold, we physically translate the sample with a motor stepper so that each individual set of measurement is performed on a fresh area. We note that all the data presented in this chapter are collected in an atmosphere of SF_6 (500 torr) as in a typical hyperdoping process.

4.3 Results

Figure 4.2 presents the reflectivity change of the silicon surface responding to single laser irradiations at different fluences. Before time zero, the reflectivity corresponds to the value for crystalline silicon at 800nm. A higher fluence results in a larger change in the reflectivity and a longer time duration for the reflectivity to return to its original value.

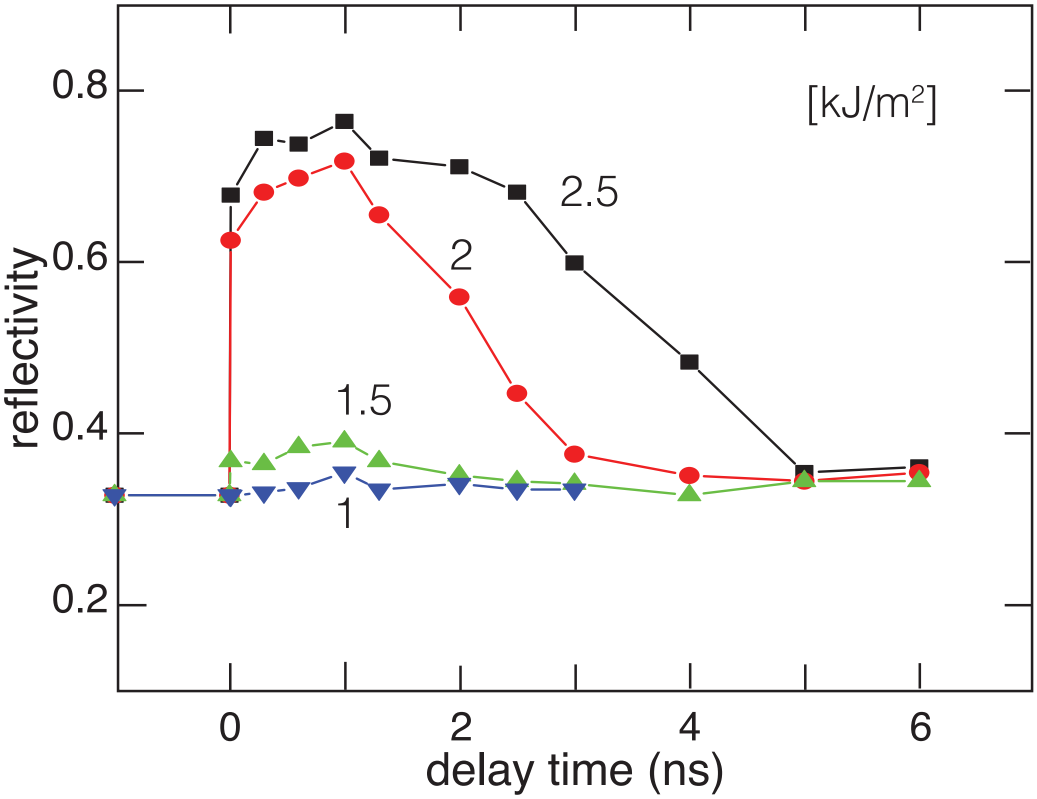

Figure 4.2: Laser-induced change in reflectivity at fluence of 1 (blue triangle), 1.5 (green triangle), 2 (red dot), and 2.5 (black square) kJ/m^2. The lines connecting the data points are for guiding the eye.

On picosecond time scales, we observe additional fine features in the data (Figure 4.3). At fluence lower than 1.25 kJ/m^2, the reflectivity decreases right after the laser irradiation then slowly recovers to its value at time zero. At 1.5 kJ/m^2, the reflectivity decreases to an even lower value compared to situations in smaller fluences. It eventually increases and reaches a value higher than crystalline silicon's reflectivity. At fluences higher than 2 kJ/m^2, the reflectivity no longer shows any decrease but increases directly after the excitation and develops a plateau after a few picoseconds. A higher fluence results in a plateau at a larger value of reflectivity.

For observing the evolution of the melt dynamics over multiple shots, we focus

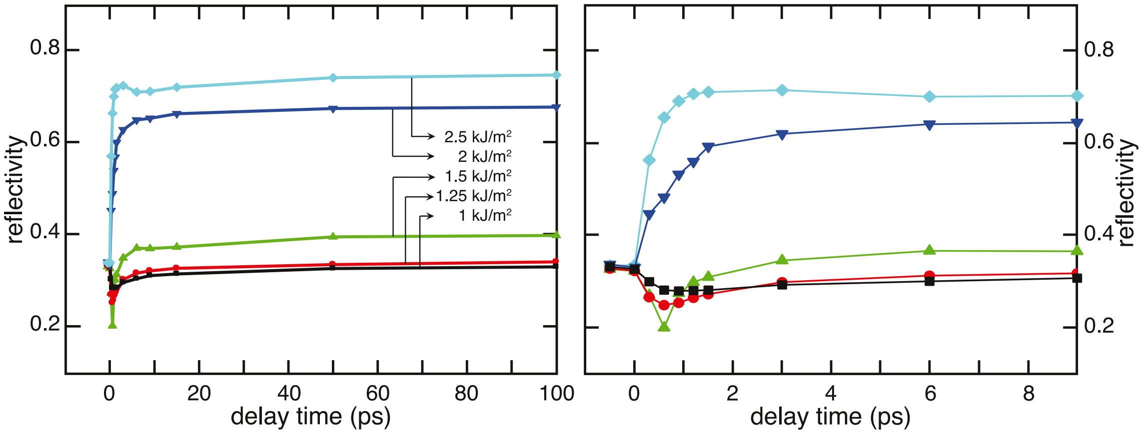

Figure 4.3: Laser-induced change in reflectivity within 100 ps (Left) and 9 ps (Right) at laser fluence of 1 (black square), 1.25 (red dot), 1.5 (green triangle), 2 (blue triangle), and 2.5 (cyan diamond) kJ/m^2. The lines connecting the data points are for guiding the eye.

on two particular fluences, 2 and 2.5 kJ/m^2, where reflectivity change is much larger than the noise (Figure 4.4). For irradiation at 2 kJ/m^2, the reflectivity increases at all delay times with increasing shots. However, the reflectivity remains the same over shots for irradiations at 2.5 kJ/m^2.

4.4 Discussion

4.4.1 Ultrafast melting

We first discuss the laser-induced change in reflectivity within 100 ps after the irradiation. When the excitation fluence is below 1.5kJ/m^2, we observe a decrease and recovery in the reflectivity in the first 10 ps. This change can be attributed to modification of the refractive index due to photo-excited electron-hole (e–h) plasma [125]. We can describe plasma's contribution to the optical property using the Drude model.

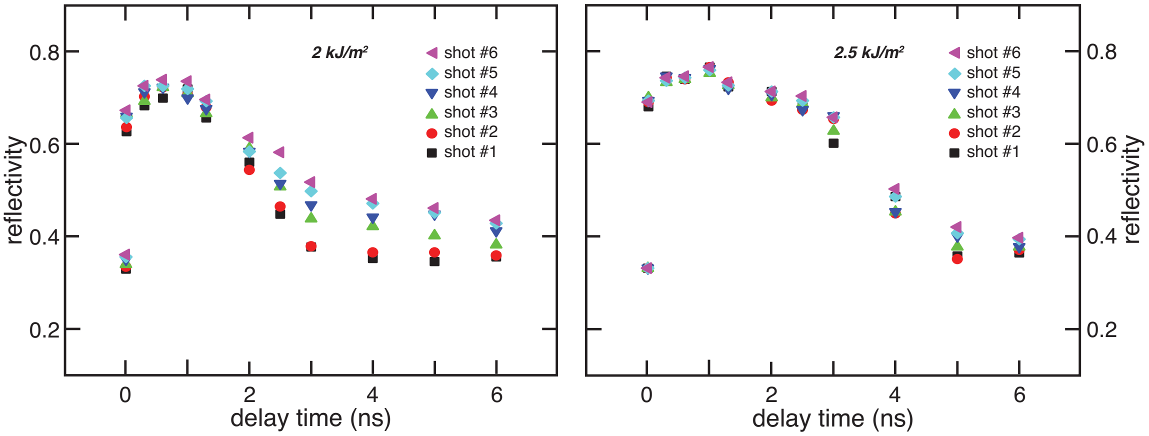

Figure 4.4: Laser-induced change in reflectivity for fluence of 2kJ/m^2 (Left) and 2.5 kJ/m^2 (Right). We perform 6 irradiations on the same area; the data is labeled as shot # 1-6, respectively.

The refractive index of the plasma (n_p) is a function of the plasma frequency (ω_p):

$$n_p^2 = 1 - \frac{\omega_p^2}{\omega^2 + i\omega\gamma}. \tag{4.1}$$

Here ω is the frequency of the probe and γ is the damping constant. The plasma frequency is a function of the plasma density (N):

$$n_p^2 = \frac{Ne^2}{m\varepsilon_0}. \tag{4.2}$$

The constants e, m, and ε_0 represent the elementary charge of electron, the effective mass of electron, and the permittivity of free space, respectively. Figure 4.5 shows the computed reflectivity of the e–h plasma for an S-polarized electromagnetic wave of a wavelength of 800 nm as a function of the plasma density. The reflectivity has a minimum when the plasma frequency reaches the probe frequency. We can estimate the carrier densities by comparing the measured reflectivity in Figure 4.3 to the predictions from the Drude model. When the fluence increases from 1 to 1.5

kJ/m^2, the lowest reflectivity corresponds to a carrier density between 1×10^{21} to 2×10^{21} cm^{-3}. We independently estimate the concentration of optically generated carriers using the following equation [120]:

$$N = F(1-R)(\alpha + \beta\frac{F(1-R)}{t})/hv. \tag{4.3}$$

Here R is the reflectivity of crystalline silicon, F is the fluence, t is the pulse duration, and hv is the photon energy. With $F = 1.5$ kJ/m^2, R = 0.33, $\alpha = 10^3$ cm^{-1}, $\beta = 9$ (cm/GW), $t = 100$ fs, and $hv = 1.55$ (eV), the estimated $N = 4 \times 10^{21}$ cm^{-3} [119]. The estimated N matches well with the value deduced from the plasma model.

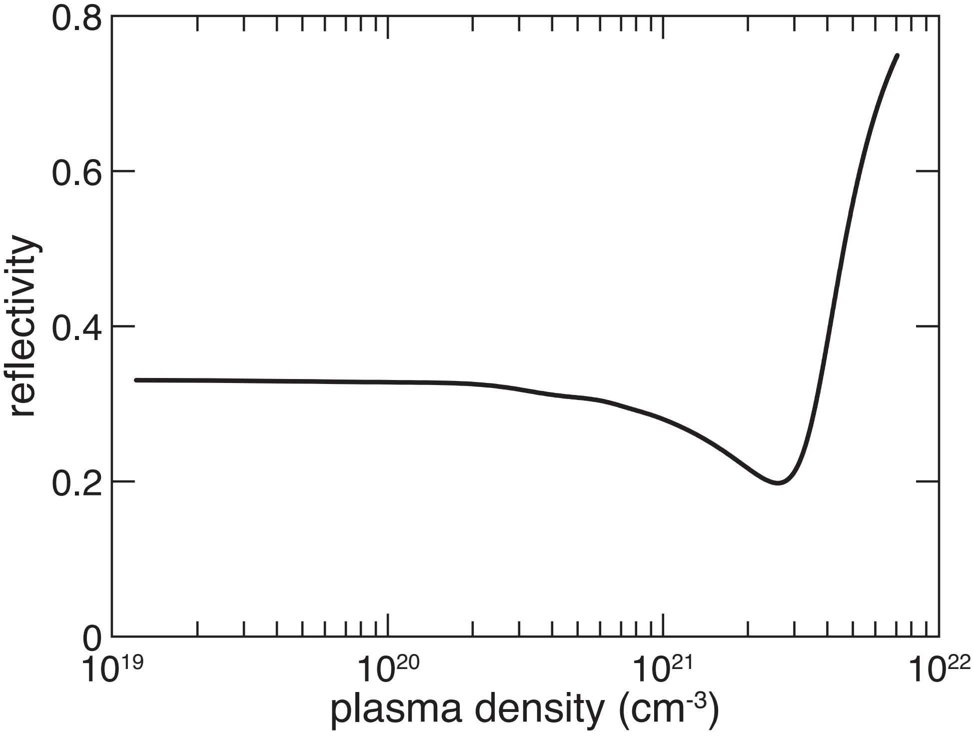

Figure 4.5: Simulated reflectivity of the e–h plasma phase as a function of the plasma density for an S-polarized electromagnetic wave having a wavelength of 800 nm. The damping constant is assumed to be 10^{15} (s^{-1}) [125].

After electronic excitation, the carriers redistribute in the conduction and the valence band through carrier–carrier scattering and carrier–phonon scattering. A few ps later, the carrier system and lattice system reach equilibrium in temperature [122]. In a classical picture, heterogeneous melting starts from the surface when the equilibrium temperature exceeds the melting temperature. To interpret the reflectivity data, we thus consider the optical properties of the following multilayer system: we assume the probe pulse interact with a layer of liquid silicon on top of the crystalline silicon substrate (Figure 4.6) [126–129]. When light arrives at the air–liquid interface, reflection and transmission occur due to a difference in refractive index of the two mediums. The transmitted part of light travels through the liquid layer and meets the liquid–solid interface. Consecutive transmission and reflection takes place at every interface. Moreover, when light travels from an optically loose material to a dense material, there is a phase shift of 180°. However, there will be no phase shift if light travels in the opposite way. As a result, interference effect gives rise to oscillations in the reflectivity as a function of liquid layer thickness. Due to the large extinction coefficient of liquid silicon, attenuation of the probe prevents it from reaching the solid-liquid interface. The probe thus carries no information about the liquid–solid interface position when the liquid layer thickness exceeds the absorption length, i.e., the property of liquid silicon dominates the reflectivity of the surface. Figure 4.7 illustrates the computed reflectivity change as a function of the liquid layer thickness.

The multilayer simulation provides us a way to estimate the melting velocity during the hyperdoping process. At a laser fluence of 2.5kJ/m^2, the melt develops a thickness of $\approx$ 30 nm in 1 ps, equivalent to a melting velocity of 30,000 m/s.

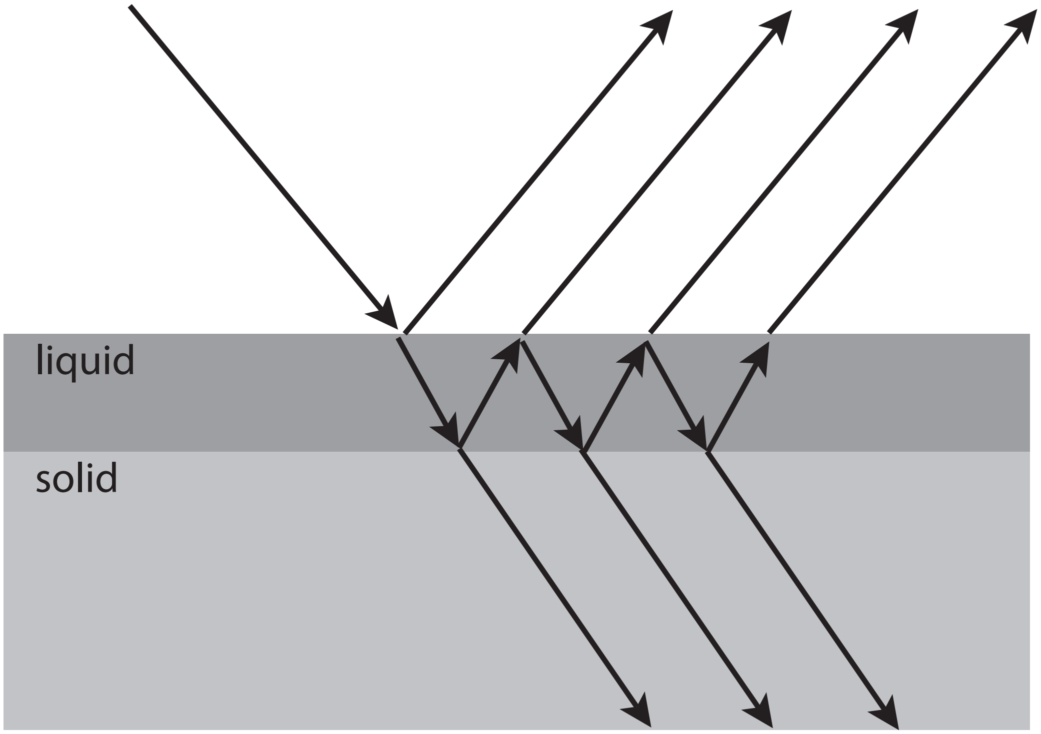

Figure 4.6: A diagram illustrating the multilayer model. The incident light refracts and reflects at each interface. The measured reflectivity is a result of interference from all light that travels to the detector.

This result is compatible with previous reports [128]. Theoretically, the maximum velocity for the heterojunction-nucleated melting is limited by the sound velocity of silicon, which is 8433 m/s along the (100) plane in silicon [115,130]. The fact that the estimated melting velocity is larger than the sound velocity implies a different physics for the melting process. Indeed, many researchers have observed short pulse induced sub-picosecond phase transition [123,131–133]. Development of the femtosecond time-resolved X-ray diffraction allows researchers to study ultrafast phase transition [120]. When a fs-laser pulse excites about 10% of the total number of valence electron to the conduction band, the lattice destabilizes within 1 ps. A “cold” liquid layer forms on the surface before electrons can transfer their energy to phonons and heat up the lattice [120, 134, 135]. The reported threshold for nonthermal melting is 2.25 kJ/m^2, matching our observation of the sub-picosecond change in reflectivity to the value of liquid silicon at 2.5 kJ/m^2 [120]. We note that although the multilayer model does not precisely describe the physics behind ultrafast melting, it provides a simplified picture that explains the experimental observation. Also, the presence of plasma could play a role in the reflectivity. However, including the plasma layer between the liquid and the solid phase does not significantly affect the simulated reflectivity, assuming the plasma density is on the order of 10^{21} cm^{-3}.

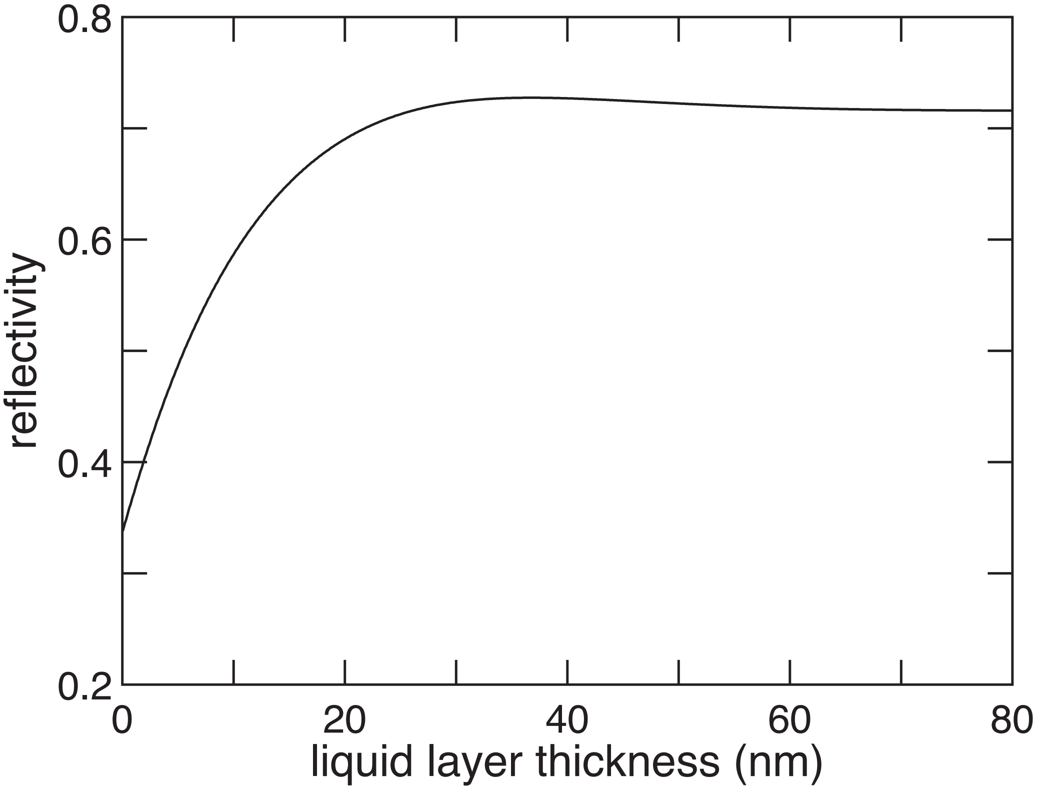

Figure 4.7: Simulated reflectivity using a multilayer model having a layer of liquid silicon on top of crystalline silicon. The polarization of light is assumed to be S-wave, matching the situation in our experiments.

The reflectivity plateau between 20 ps and 100 ps for 2.5 kJ/m^2 corresponds to the reflectivity of liquid silicon because the liquid silicon thickness exceeds 30 nm. However, for 1.25 and 1.5 kJ/m^2, the reflectivity does not exceed the value for molten silicon. This implies that the melt depth is smaller than 30 nm and the interface stays nearly where it is between 20 ps to 100 ps. Gundrum *et al.* reported similar phenomenon by probing the liquid–solid interface movement using the third harmonic generation method. Their experiment also suggests that the interface stagnates for up to hundreds of picoseconds [136]. Although we do not fully understand the physical mechanism behind this phenomenon, we speculate that the high *e*–*h* density in the substrate prevents heat transfer from the liquid to the substrate because phonon-phonon coupling could be screened.

4.4.2 Melt duration and resolidification velocity

We discuss the reflectivity change on a nanosecond time scale in this section. When the laser fluence is above the melting threshold, the time it takes for reflectivity to recover to its original value before irradiation indicates the melt duration, i.e. the time during which a liquid layer exists at the surface of silicon. As seen in Figure 4.2, the melt duration is about 3 ns and 5 ns for 2 kJ/m^2 and 2.5 kJ/m^2, respectively. We again apply the multilayer model to measure the liquid layer thickness as a function of time and extract the resolidification velocity. The plasma no longer exists when resolidification starts after hundreds of picoseconds. Therefore, it is reasonable to assume only a layer of liquid on top of the silicon substrate in the model. We perform least squares fitting to the experimental data assuming a constant resolidification velocity. In Figure 4.8 we plot the experimental data and simulated reflectivity for

2 kJ/m^2 and 2.5 kJ/m^2. The resolidification velocity is 12 and 10 m/s for 2 kJ/m^2 and 2.5 kJ/m^2, respectively. We then compare our experimental observation to the previous work on fitting the experimentally obtained doping profile with the adapted model [124]. The fitting parameter for the adapted model is the nonlinear absorption coefficient and the effective fluence. These two values affect the melt duration and the resolidification velocity; thus determine the overall doping profile. Here, the boundary condition at the liquid–solid interface is assumed to be following the kinetics of solute trapping developed for the ns-laser melting. At 2.5 kJ/m^2, the fitted melt duration and the resolidification velocity from the adapted model agree well with our experimental results obtained by the pump-probe measurements. This implies that the simplified classical model can describe the result of fs-laser hyperdoping despite nonthermal melting could dominate over heterogeneous melting. Specifically, the classical model produces the correct doping profile only when the resolidification dynamics is close to the actual situation.

For various laser pulses applied to the same surface area, the reflectivity evolution over multiple laser irradiations has distinct trends in two fluence regimes. At 2 kJ/m^2, the reflectivity increases over shots at all time delay. We can reproduce the reflectivity data only if a layer of amorphous silicon is included in the multilayer model. Indeed, optical image of the irradiated area appears to be pink, agreeing with our speculation that a layer of amorphous silicon covers the surface of silicon substrate. Raman spectrum further confirms this assumption. As shown in Figure 4.9, the resolidification velocity increases from 12 m/s to 16 m/s after 6 laser irradiations. It was reported that silicon experience phase transition when the reso-

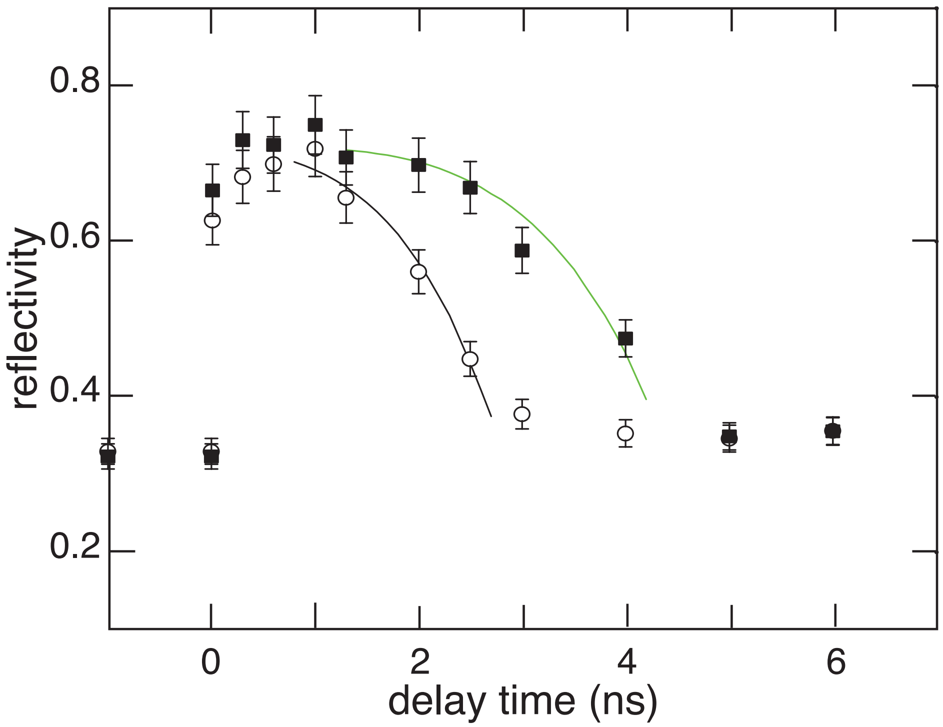

Figure 4.8: Reflectivity change under laser irradiation of 2 kJ/m^2 (open circles) and 2.5 kJ/m^2 (solid squares). The black curve and green curve correspond to the simulated reflectivity change with a constant resolidification velocity of 12 m/s and 10 m/s, respectively.

lidification velocity exceeds 15 m/s [137]. We hypothesis that the phase transition from crystalline to amorphous occurs due to lattice defects accumulates upon each laser melting and resolidification cycle. Heat deposition thus varies for each irradiation and the resolidification dynamics changes as a result. Future investigation on the defect concentration and the amorphous layer thickness could provide insight for explaining this phenomenon.

We attribute the additional long tail in reflectivity after 2.5 ns in the 6 shots sample to the change in temperature while the surface cools down from nearly the melting temperature to room temperature after resolidification. The presence of

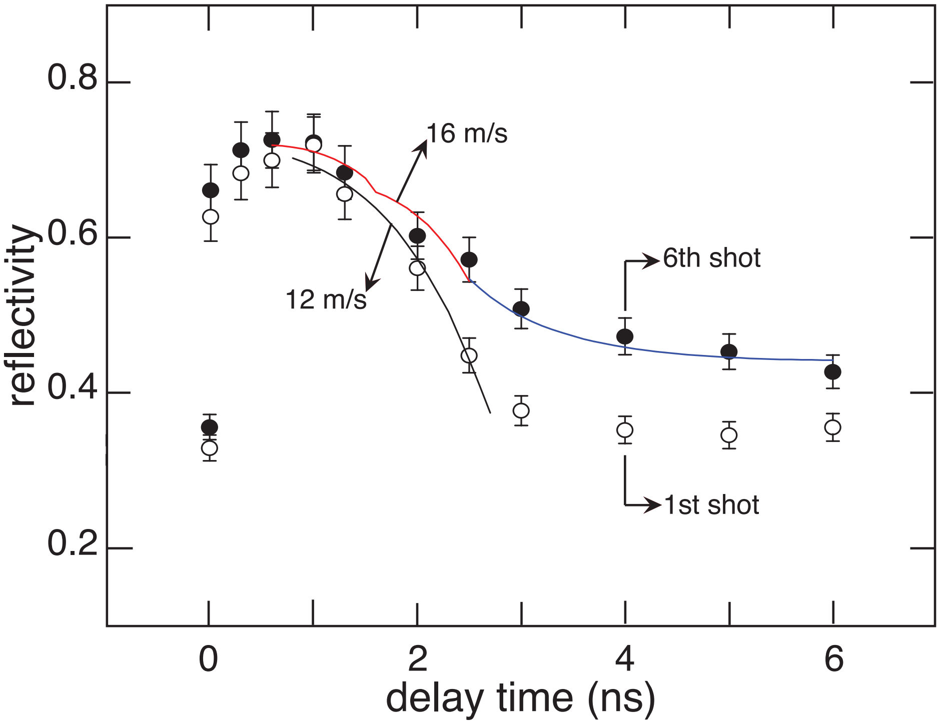

Figure 4.9: Reflectivity change under laser irradiation of 2 kJ/m^2 (open circles) and 2.5 kJ/m^2 (solid squares). The black curve and green curve correspond to the simulated reflectivity change with a constant resolidification velocity of 12 m/s and 10 m/s, respectively.

heated amorphous silicon creates a difference in the index between the amorphous layer and the silicon layer underneath [138]. Since amorphous silicon has a much stronger extinction coefficient than silicon, the effective surface reflectivity can be higher than 0.5 when the temperature is near the melting point. As heat diffuses into the bulk, the temperature and the reflectivity decreases concurrently. We fit the tail assuming an exponential decay in temperature (blue curve in Figure 4.9). Solving the actual temperature decay with the Green's function method provides deeper insight into how the surface temperature evolves over time. The result suggests that the temperature decay has the same time constant as the fitted curve in the beginning of the heat diffusion. The total time it takes for heat to diffuse away is however on the order of hundreds of nanoseconds. This time scale is consistent with our separate experiment where we use a continuous-wave laser as the probe beam to record the reflectivity change up to a microsecond.

At 2.5 kJ/m^2, the reflectivity remains almost the same value upon multiple irradiations at any time delay. This is implying a repeatable melt dynamics up to 6 irradiations at the same fluence. Previously, Sher *et al.* performed secondary ion mass spectrometry (SIMS) measurements on a series of silicon wafers doped with different number of laser irradiations at 2.5 kJ/m^2 [139]. Fitting the SIMS profiles with the classical model provided two approaches to reproduce the SIMS profiles: 1) the boundary condition at the surface changes from diffusive to instant dose over shots, and 2) the melt duration increases over shots. Our independently performed pump-probe experiments suggest that the melt dynamics remains unchanged up to 6 shots and rules out the second hypothesis [124].

Our finding not only provides an answer to the previously unresolved puzzle but also validates the assumptions made in the numerical model. In the numerical model, the interface response function, the interface velocity as a function of the interface temperature, is one important boundary condition at the solid-liquid interface for solving the heat equations. For previous simulations, the interface response function is assumed to be in the linear regime throughout the hyperdoping process. This assumption can be critical to the validity of the numerical model since fs-laser produces a highly nonequilibrium condition that could drive the interface response function to the nonlinear regime. Furthermore, the numerical model does not take into account of possible nonthermal melting that is easily achieved by fs-laser pulses. Instead, the model assumes a certain thickness of molten silicon after a short period of time (0.5 ns). Our pump-probe reflectivity measurements provide direct observation of the melt duration and resolidification velocity that matches with the simulated scenario from fitting the SIMS results by varying the nonlinear absorption coefficient and the laser fluence. The consistency between experiments and simulations assures one thing: our assumption for the interface response function is valid and how the materials melt does not affect the classical picture during the hyperdoping process. The robustness of the numerical model opens an avenue for further engineering design using femtosecond-laser hyperdoping, as we will discuss in the next chapter.

4.5 Conclusion

In this chapter, we achieve in answering the following questions: 1) what is the melt duration and resolidification velocity? 2) how can we control the resolidification velocity. We demonstrate a pump-probe technique that measures the liquid–solid interface position during fs-hyperdoping. Using a multilayer model, we extract the interface movement and reach several conclusions. First, the melt duration is on the order of nanosecond for hyperdoping using a laser fluence below the ablation threshold. The melt duration increases from 3 ns to 5 ns with increasing laser fluence from 2 $\mathrm{kJ/m^2}$ to 2.5 $\mathrm{kJ/m^2}$. Second, although fs-laser induced melting could have different mechanism from ns-laser melting, the resolidification velocity in both cases is on the order of 10 m/s. Thus, it is reasonable to predict the doping profile with a numerical model based on classical descriptions of heat and solute transport and solute trapping. We will apply this method to design doping profile in the next chapter. Third, we can control the crystallinity of the hyperdoped silicon with laser fluence. A lower fluence induces a faster resolidification velocity that promotes phase transition from crystalline to amorphous during resolidification. Our contribution in understanding the melt dynamics allows further engineering to obtain desired materials qualities.

Chapter 5

Designing the hyperdoping profiles

In this chapter, we present a fabrication process that produces hyperdoped silicon of a homogeneous doping profile based on our understanding of the dynamics of melting and resolidification and the development of a numerical model that simulates the doping profiles. This work is in collaboration with Niall Mangan, Sophie Marbach, and Tobias Schneider from the Brenner group at Harvard University.

5.1 Introduction

Optical and electronic properties of silicon are controlled by the concentration of dopants. Traditionally the impurities are incorporated during the slow growth of silicon crystals from its melt. Here dopant concentrations are limited to the equilibrium solubility limit in the solid. Non-equilibrium processes such as laser-hyperdoping can achieve much higher concentrations. Irradiating silicon with intense fs-laser pulses in a sulfur-containing atmosphere allows surpassing the equilibrium concentration limit by up to four orders of magnitude [41]. At sulfur concentrations of up to 1 at.%, the band structure fundamentally changes [111, 140]. Overlapping sulfur donor states potentially create an additional metallic intermediate band which allows for two sub-band gap IR photons to excite an electron to the conduction band [63, 64]. With its IR absorption capability, hyperdoped silicon is of interest for new devices such as silicon-based IR detectors and highly efficient photovoltaic cells harvesting the IR spectrum without reducing the band gap [59, 141].

Femtosecond-laser hyperdoping greatly expands the range of accessible dopant concentrations yet the high concentration profiles achieved typically have a sharp decay on a length scale a hundred nanometers when moving from the surface into the bulk material. The resulting non-homogeneous material properties raise the question: Can we control the doping process and generate a flat profile of doping concentration up to a given depth?

Despite the extreme energy fluxes involved in fs-laser treatment the dopant incorporation mechanism appears dominated by classical heat and solute diffusion coupled to a very-far-from equilibrium phase change during melting and resolidification [124]. When a laser pulse of 100 femtoseconds and a fluence of 3 $\mathrm{kJ/m^2}$ hits silicon, the non-reflected part of the light energy is absorbed by the carrier system. On a timescale fast compared to all other transport timescales the silicon lattice melts. Sulfur ions from the gas atmosphere now diffuse into the liquid surface layer and are incorporated when the silicon cools and resolidifies. The key is the extremely high intensity of 10^{12} $\mathrm{W/m^2}$ of the laser pulse causing nonlinear absorption of the energy in a very thin surface layer, resulting in extreme thermal gradients of 109 K/m. The released latent heat of the solid-liquid phase change during resolidification is thus transported away very quickly. The phase change is driven to extremely far-from-equilibrium conditions while the resolidification front moves at velocities of several meters per second. This velocity is large compared to the diffusive velocity at the interface ($V_{DI} = 1$ m/s) at which sulfur ions can jump from the solid phase back to the liquid phase [54]. Consequently, instead of being rejected like salt from slowly freezing seawater, the solute is "trapped" in the solid, giving rise to greatly enhanced dopant concentrations.

We emphasize a key step in this presumed picture of hyperdoping: solute diffusion in the liquid phase during the doping process. If the dopants indeed transport diffusively in the liquid phase, we can utilize this mechanism to eliminate the concentration gradient by providing enough diffusion time for the dopants to pile up at the melt depth. A series of simulated doping profiles presented in Figure 5.1 provides an intuitive understanding of how to achieve a flat doping profile with the aid of diffusion. This simulation is performed based on a melt dynamics verified by our previous pump-probe experiments and assuming the presence of a dopant flux only during the first laser doping cycle. In this chapter, we demonstrate a doping process that achieves an almost rectangular profile by maximizing the dopant diffusion time and minimizing the melt depth. Our study of the profile evolution from shot to shot provides a direct observation of the doping mechanism.

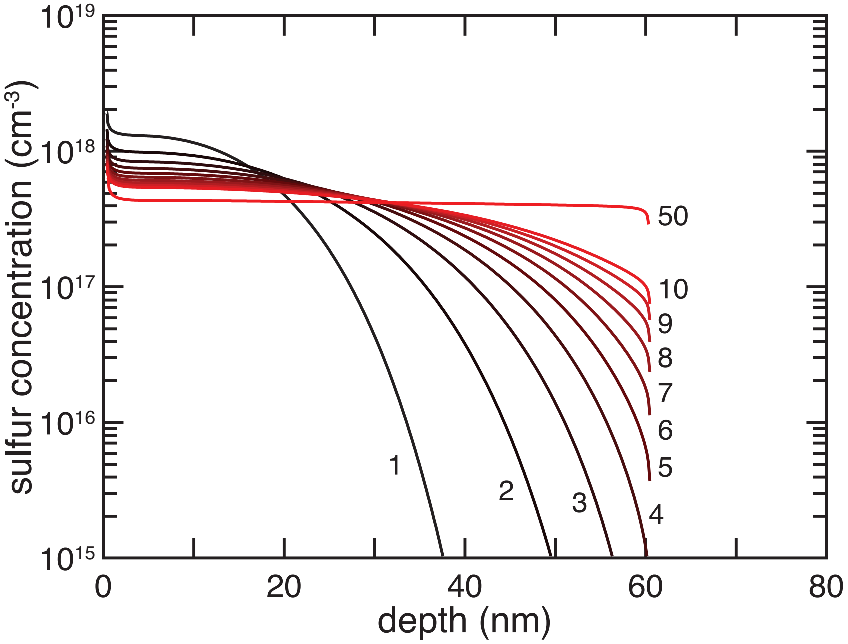

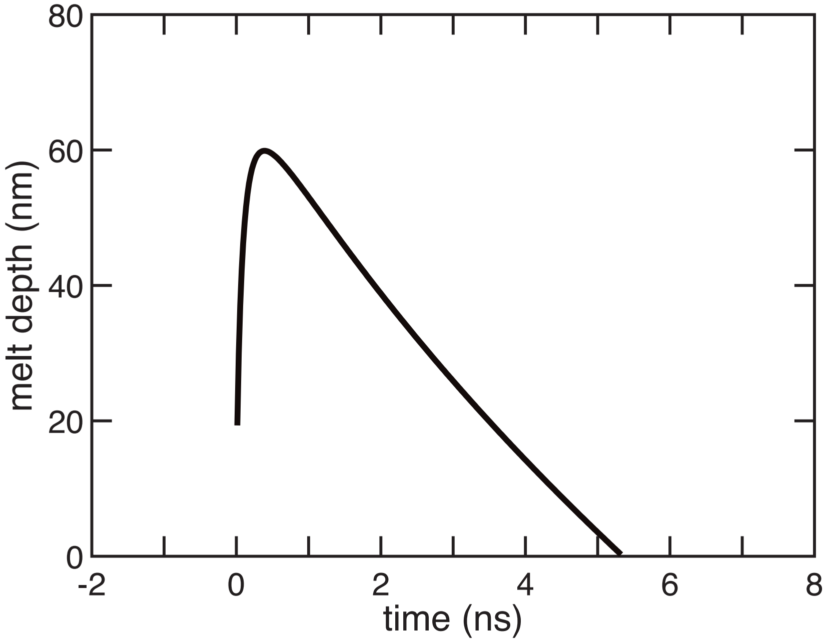

Figure 5.1: (Top) The simulated doping profile evolution from 1 to 50 laser shots at the same fluence. The sulfur flux is only present in the first shot. (Bottom) The melt dynamics used for the simulation.

5.2 Experimental

Ideally, one can fabricate a flat doping profile at any fluence by using an infinite number of laser shots. In reality, we need to take into account several limiting factors when designing the experiment. First of all, a flat surface is desirable for quantitative analysis to study the doping profile with secondary ion mass spectrometry (SIMS). However, nano-scale surface periodic structures would appear after a few laser irradiations [39, 142]. The actual number depends on the laser fluence chosen, the atmosphere, and the surface condition of the wafer. To achieve a flat profile, we should thus select a fluence that maximize the integrated diffusion time for the dopants to transport down the concentration gradient and pile up at the melt depth. Secondly, the resolidification velocity increases with decreasing fluence, leading to higher concentrations of lattice defect in the resolidified region. Eventually, the interface moves faster than the time required for atoms to find a lattice site to sit in, resulting in amorphization. This transition velocity is found to be 15 m/s in literature [137]. Laser induced lattice defects also facilitate the formation of surface structures. As a result, it takes less shots to create surface structures at lower fluence. Lastly, the laser fluence must be smaller than the ablation threshold [97]. Otherwise, significant material removal and unavoidable surface roughness complicate the SIMS measurements and data analysis.

We use a regeneratively amplified Ti:sapphire laser system to hyperdope silicon at a repetition rate of 100 Hz. No thermal footprint is accumulating since it takes less than 1 ms for silicon to cool down to room temperature. The elliptical laser pulse has a bandwidth centered at 810 nm, a pulse duration of 70 fs as measured with an autocorrelator. With a combination of a half waveplate and a polarizer, we tune the average pulse energy to 0.87 mJ and then focus it to a full-width at half-maximum of 945×1135 μm as measured with a CCD camera. The effective fluence is 2.7 kJ/m^2, above the melting threshold (1.5 kJ/m^2) and below the ablation threshold of silicon (3 kJ/m^2) [97, 143]. We select this fluence because it allows the maximum number of irradiation before any surface structures form on the surface.

Before hyperdoping, the silicon wafer (Boron doped, resistivity=7-14 Ω·cm) is patterned by a standard photolithography procedure using a positive resist, Shipley S1818, and dry-etched with a reactive ion etch to form circular mesas having a diameter of 800 μm and a height of 2 μm. These mesas serve for alignment purposes in the hyperdoping process and SIMS measurements later on. We clean the patterned wafer with acetone, methanol, isopropanol, and water before placing in a vacuum chamber. The chamber is pumped down to 10^{-6} torr then back-filled with 730 torr of SF_6. We use a mechanical shutter to control how many pulses irradiate onto the silicon wafer to fabricate a set of hyperdoped silicon following the design principle suggested by the numerical simulation. We are able to irradiate 9 laser pulses without creating any surface structures, suitable for precise SIMS measurements. The crystallinity and surface morphology are examined by Raman spectroscopy and optical profilometry. We label samples from 1 to 9 to indicate how many laser shots are performed. The first laser shot of all samples is done in 730 torr of SF_6. All the subsequent shots in sample 2 to 8 are done in vacuum (10^{-6} torr). As an example, sample 9 is irradiated by 1 laser shot in SF_6 followed by 8 laser shots in vacuum.

We carried out SIMS measurements with a Cs ion beam of 6 keV at a current of 7 nA. We align the ion beam to the center of the laser-irradiated area. The ion beam is focused to a spot size of 150 × 200 μm. We collect only the center 15x30 μm of secondary ion signals by electronic gating, an area corresponding to less than 1 % of fluence variation in a Gaussian pulse used for fabrication. We monitor ion channels including ^{29}Si, ^{32}S, ^{34}S, and ^{18}O. We use a sulfur standard (dose=1×10^{14} cm^{-2}) made by ion implantation for calculating the relative sensitivity factor.

5.3 Result

In Figure 5.2, we show the experimentally measured sulfur concentration depth profiles of the designed sample set. For clarity, we show only a selective data set of samples made with 5 different shot numbers. The concentration profile for sample 1 shows an exponential decay over depth. A plateau develops gradually with increasing shot number. Sample 9 shows a flat profile over depth up to about 55 nm. We cut off the first 6 nanometers of the data because it takes time to develop a stable drilling rate in SIMS and thus reliable ion counts. The noise level is at about 10^{16} cm^{-3}. An exponential tail having a decay rate of 10 nm per decade exists in all samples.

In Figure 5.3, we compare the numerical simulation and the experimental results for sample 9. We point out a few consistencies and discrepancies for further discussions here. First of all, both the SIMS profile and simulated profile show a peak in concentration near the surface. Secondly, the depths where the simulated and measured profiles cut off are within the experimental error of SIMS. Furthermore, the experimental curve is flatter than the simulated curve. Figure 5.4 shows the total sulfur dose, integration of the concentration profile over depth, for each sample.

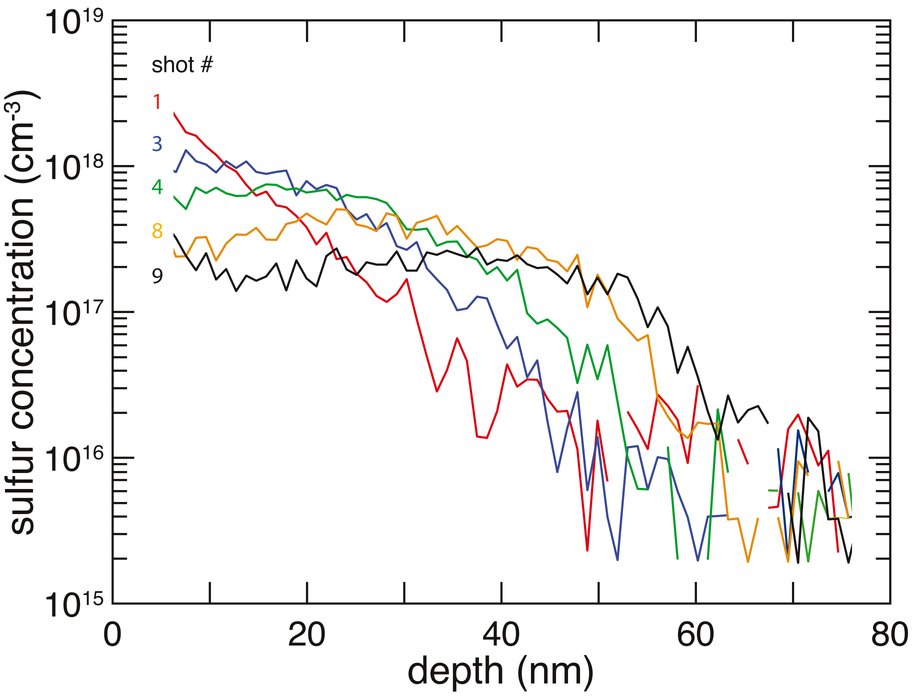

Figure 5.2: Evolution of SIMS profiles of the hyperdoped samples from shot 1 to 9. We select only these shot numbers for clarity. The profile changes from an exponential decay in the first shot to a nearly flat profile in the 9^{th} shot.

5.4 Discussion

The evolution of SIMS profiles from shot to shot is a direct observation of the diffusive behavior of dopants that are incorporated in the first laser pulse. This result shed light on one important question: are there other physical mechanisms additional to diffusion and solute trapping necessary for achieving hyperdoping? Since the dopant source is cut off after the first laser pulse, evolution of the doping profiles reflects the dominating physical mechanism during hyperdoping. Despite the experimental limitations that result in a 10-nm uncertainty in depth [144], the evolution of the SIMS

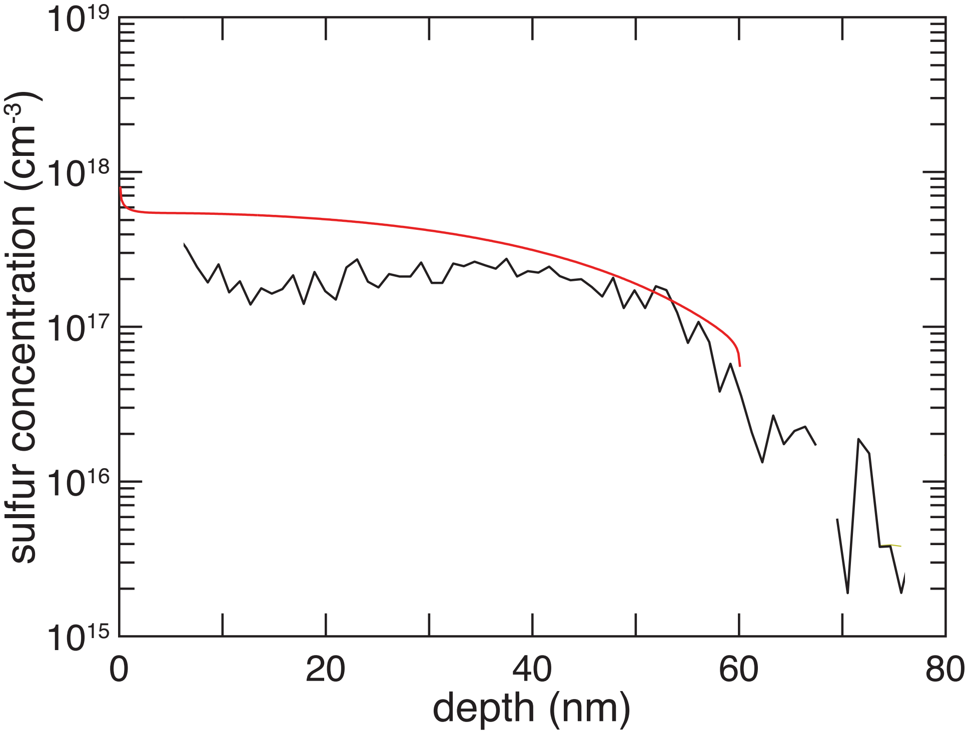

Figure 5.3: Comparison of the simulated (red) and measured (black) profile for the 9th shot sample.

profiles is consistent with the simulated results presented in Figure 5.1. Following the principle of solute diffusion coupled to the far-from-equilibrium phase transition, the sulfur concentration gradient introduced in the first laser shot is smeared out by subsequent shots. This is indeed a strong proof that diffusion is the dominating process for solute transport during hyperdoping, eliminating other possibilities such as active ion implantation due to presence of a plasma phase at the surface.

We successfully obtain a nearly flat profile with 9 laser irradiations, which is less than the prediction in the simulation. This discrepancy provides us with more insights on the actual doping process. If we compare the SIMS profile to the simulated

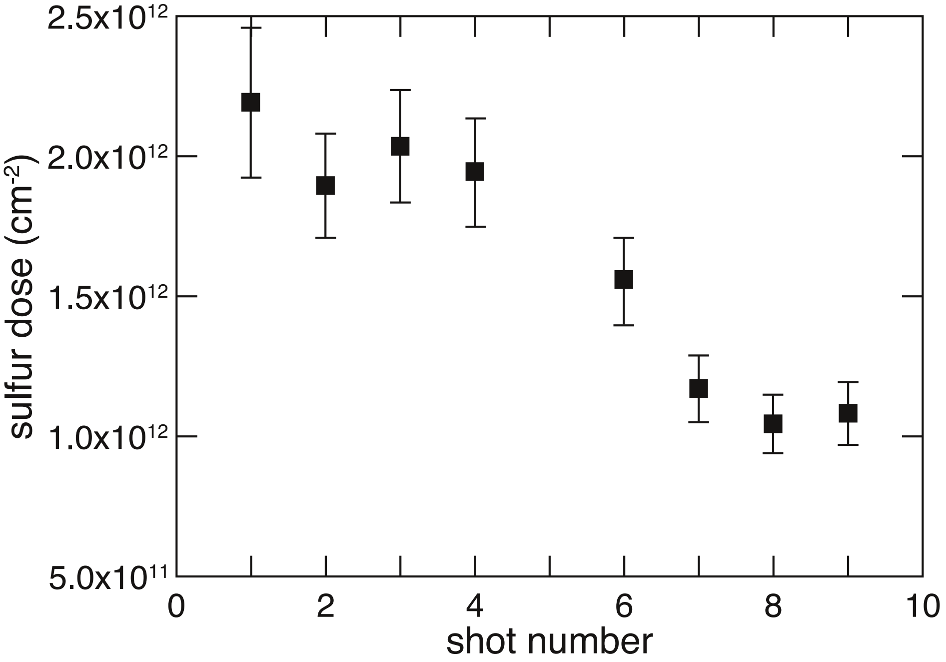

Figure 5.4: Evolution of the sulfur dose over laser irradiations from 1 to 9 shots.

profile, the decrease in sulfur concentrations near the surface shows an evidence for evaporation of sulfur at the surface. This is confirmed by integrating each SIMS profile to obtain the total sulfur dose as a function of laser shot (Figure 5.4). After three laser shots, a monotonic decrease in the sulfur dose indicates an outward flow of sulfur after the native oxide layer evaporates and/or diffuses into the silicon bulk. Secondly, since the resolidification velocity is finite, sulfur gets rejected from the solid phase and accumulates in front of the moving interface. Without an outward flux that releases the sulfur pile-up near the end of the resolidification, the simulation predicts a steep sulfur concentration slope at the surface that requires a longer integrated diffusion time to be erased.

Table 5.1: The diffusion length for each laser shot and the integrated diffusion length after certain shot number calculated assuming the melt duration is 5 ns, the resolidification velocity is 12 m/s, and $D = 2.7 \times 10^{-4}$ cm^2/s [65].

Shot number	Diff. length (nm)	Integrated diff. length (nm)
1	12.2	12.2
2	10.9	23.1
3	9.60	30.6
4	8.23	40.9
5	6.88	47.7
6	5.51	53.2
7	4.09	57.3
8	2.57	59.9
9	4.88	60.4

We believe the sulfur ions have reached the melt depth based on our estimation of the integrated diffusion length using $\sqrt{Dt}$, where D is the diffusivity of sulfur in liquid silicon and t is the diffusion time. From the simulation (Figure 5.1), the melt dynamics has a nearly triangular shape that provides less and less diffusion time as the dopants enter deeper and deeper into the melt. Assuming $D = 2.7 \times 10^{-4}$ cm^2/s and the melt duration and resolidification velocity is 5 ns and 12 m/s as deduced from the simulated melt dynamics from Figure 5.1, we calculate the integrated diffusion length as a function of laser shots [65]. As listed in Table 5.1, the integrated diffusion length after 9 shots has a value of $\approx$ 60 nm, which approaches the assumed melt depth seen in Figure 5.2. This estimation assures our hypothesis that the dopants has reached the melt depth and piled up to form a flat profile.

Lastly, we note that the exponential tails observed in all samples are due to a mixing effect, Cs ions implanting sulfur ions into the sample rather than sputtering them off the surface. A concentration profile measured on a reference area that has not been irradiated by any laser pulses (not shown) shows the same decaying signals coming from ionized oxygen due to the presence of native oxide at the silicon surface.

5.5 Conclusion

We have successfully fabricated hyperdoped silicon of homogeneous doping concentrations over depth with a designed doping sequence that maximizes the diffusion time for solute to pile up at the melt depth. Furthermore, our work provides the direct experimental proof to the assumption that diffusion is the dominating solute transport mechanism during hyperdoping as opposed to other possible processes such as active ion implantation driven by the laser induced electron-hole plasma. This work demonstrates the feasibility to design and fabricate hyperdoped silicon on demand with our deep understanding of the hyperdoping process.

Chapter 6

Summary and future directions

In this thesis, we present efforts into advancing the field of photovoltaics research with two femtosecond-laser processing methods: 1) surface texturing — transform flat surfaces into randomly textured landscapes that are perfect for enhancing absorption in thin materials through anti-reflection and light-trapping, and 2) hyperdoping — introduce non-equilibrium amount of deep level dopants to create an intermediate band material that absorbs sub-bandgap photons without sacrificing the voltage of a device.

In Chapter 2 we review the history of "black silicon" and its applications to photovoltaics. Black silicon was first discovered as an unwanted side effect during reactive ion etching processes. The Mazur group discovered another kind of Black Silicon of spiky surface morphology when irradiation silicon with femtosecond-laser pulses in an ambient filled with SF_6.

In chapter 3, we fabricate light-trapping thin silicon surfaces with femtosecond-laser pulses and demonstrate an enhancement in the external quantum efficiency and the short circuit current of our light-trapping solar cells. Our femtosecond-laser technique effectively transforms flat silicon surfaces into random textures that scatter incident photons like a Lambertian surface. Unfortunately, concurrent with the surface texturing, the extreme temporally- and spatially-confined energy flux results in structural damages underneath the silicon surface. We thus apply an additional wet etching step to remove the laser-induced damage layer. For the future, we suggest two ways to further improve our current processes. First, we suggest texturing the silicon surface in different environments other than H_2. Texturing in SF_6 is one choice because we expect fluorine ions to etch away the surface and results in a thinner damaged layer. We might be able to preserve better the laser textures after the subsequent chemical etching process. Texturing under water could be another choice. We expect formation of silicon dioxide during the processing, which is desirable because a simple oxide removal etchant such as HF solution might be able to replace our two-step etching recipe. Second, we suggest annealing the textured surface with nanosecond-laser melting techniques to recrystallize the damaged layer. Previously, we have tried annealing the textured surface with an oven. However, the process cannot remove all the lattice defects under a reasonable annealing temperature and time duration. One benefit of using a nanosecond-laser is that it produces a fast melting and resolidification process to maintain the surface morphology yet a slow enough resolidification velocity for the molten layer to epitaxially recrystallize. Also, a longer pulse compared to our femtosecond-laser pulses minimizes the amount of ablation occurring at the valleys of the surface morphology where light is preferentially focused. Nevertheless, the uniqueness of the nanometer-sized surface morphologies we create with femtosecond-laser pulses cannot be easily achieved by nanosecond-lasers. Therefore, for applications to thin film solar cells, combination of these two processing tools of different merits might be promising.

In chapter 4, we study the hyperdoping mechanism by probing the silicon surface reflectivity in situ during the hyperdoping process. Our work contributes to the understanding of the laser-induced ultrafast melting and resolidification process, the melt dynamics, which is essential for modeling the doping process. We find out two distinct laser fluence regimes where the melt dynamics either evolves over shots or remains the same. The silicon surface transforms into amorphous over shots in the former case, while the crystallinity remains unchanged in the later case. These observation and analysis are crucial for engineering the hyperdoping process because typically it requires multiple irradiations to manipulate a doping profile. We have spent much effort in incorporating the pump-probe spectroscopy into our laser fabrication system. The current setup is suitable for studying a variety of ultrafast processes such as carrier dynamics in any material systems. For future upgrade of the apparatus, we suggest changing the current chamber into a larger one to grant more space for different types of measurements including high-angle reflection and transmission measurements.

In chapter 5, we utilize our understanding of the melt dynamics and ways to control the crystallinity and the surface morphology to fabricate hyperdoped silicon of a designed doping profile. With the aid of a numerical model verified by our knowledge in the melt dynamics, we have successfully designed and fabricated hyperdoped silicon with a homogeneous doping profile throughout the molten surface layer. Although the doping concentration is nearly constant in the doped layer, the absolute value of it is not large enough for the insulator-to-metal transition to occur. However, the mature development of this technique allows further applications to different material systems.

The Mazur group's work in femtosecond-laser texturing and hyperdoping started in a serendipitous way back in 1998 when Black Silicon was discovered unexpectedly during experiments on surface chemistry. Over the past 16 years we have been making efforts to understand the material properties our laser-processed materials and apply them to usable devices such as solar cells and photodetectors. A spin-off company from our group, SiOnyx, is continuing to apply our laser processing methods in making commercially available products. To me, the future of our texturing and hyperdoping is promising and I hope our work provide inspiration to researchers in studying different material systems and applications.

Bibliography

[1] D. M. Powell, M. T. Winkler, H. J. Choi, C. B. Simmons, D. Berney Needleman, and T. Buonassisi, Energy & Environmental Science **5**, 5874 (2012).

[2] Eicke R. Weber, Applied Physics A Solids and Surfaces **30**, 1 (1983).

[3] D. M. Chapin, C. S. Fuller, and G. L. Pearson, Journal of Applied Physics **25**, 676 (1954).

[4] H. W. Lehmann, Journal of Vacuum Science and Technology **14**, 281 (1977).

[5] R. Kassing I. W. Rangelow, P. Thoren, K. MaBeli, Microelectronic Engineering **5**, 387 (1986).

[6] Gottlieb S Oehrlein, Robert G Schad, and Mark A Jam, Surface and Interface Analysis **8**, 243 (1986).

[7] R. Thomas, D. J.; Southworth, P.; Flowers, M.C.; Greef, Journal of Vacuum Science & Technology B: Microelectronics and Nanometer Structures **7**, 1325 (1989).

[8] J. I. Gittleman, E. K. Sichel, H. W. Lehmann, and R. Widmer, Applied Physics Letters **35**, 742 (1979).

[9] J.S. Yoo, I.O. Parm, U. Gangopadhyay, Kyunghae Kim, S.K. Dhungel, D. Mangalaraj, and Junsin Yi, Solar Energy Materials and Solar Cells **90**, 3085 (2006).

[10] Sameer Chhajed, Martin F. Schubert, Jong Kyu Kim, and E. Fred Schubert, Applied Physics Letters **93**, 251108 (2008).

[11] Henri Jansen, Han Gardeniers, Meint De Boer, Miko Elwenspoek, and Jan Fluitman, Journal of Micromechanics and Microengineering **6**, 14 (1996).

[12] Patrick Campbell and Martin a. Green, Journal of Applied Physics **62**, 243 (1987).

[13] Kirt R Williams, Senior Member, Kishan Gupta, Student Member, and Matthew Wasilik, journal of microelectromechanical systems **12**, 761 (2003).

[14] V. La Ferrarab P. Menna, G. Di Franciaa, Solar Energy Materials and Solar Cells **37**, 13 (1995).

[15] E. Bucher P. Fath, G. Willeke, Photovoltaic Energy Conversion 1347 (1994).

[16] Jianhua Zhao, Aihua Wang, Martin a. Green, and Francesca Ferrazza, Applied Physics Letters **73**, 1991 (1998).

[17] Zhipeng Huang, Nadine Geyer, Peter Werner, Johannes de Boor, and Ulrich Gösele, Advanced materials **23**, 285 (2011).

[18] Barada K Nayak, Vikram V Iyengar, and Mool C Gupta, Progress in Photovoltaics: Research and Applications **19**, 631 (2011).

[19] A. Kumaravelu, G., Alkaisi, M.M., Bittar, Photovoltaic Specialists Conference 258 (2002).

[20] James E Carey, Catherine H Crouch, and Eric Mazur, Optics and Photonics News 32 (2003).

[21] Adela Ben-Yakar, Robert L. Byer, Anthony Harkin, Jacqueline Ashmore, Howard a. Stone, Mengyan Shen, and Eric Mazur, Applied Physics Letters **83**, 3030 (2003).

[22] Thomas R Polte, Mengyan Shen, John Karavitis, Martin Montoya, Jay Pendse, Shannon Xia, Eric Mazur, and Donald E Ingber, Biomaterials **28**, 2783 (2007).

[23] Cong Wang, Haibin Huo, Michael Johnson, Mengyan Shen, and Eric Mazur, Nanotechnology **21**, 75304 (2010).

[24] Gottlieb S. Oehrlein, Physics Today **39**, 26 (1986).

[25] H V Jansen, M J de Boer, S Unnikrishnan, M C Louwerse, and M C Elwenspoek, Journal of Micromechanics and Microengineering **19**, 033001 (2009).

[26] G. C. Schwartz, Journal of Vacuum Science and Technology **16**, 410 (1979).

[27] G. C. Schwartz, L. B. Rothman and T. J. Schopen, J. Electrochem. Soc 464 (1979).

[28] Henri Jansen, Meint De Boer, Rob Legtenberg, and Miko Elwenspoek, Journal of Micromechanics and Microengineering **5**, 115 (1995).

[29] G. S. Oehrlein, Journal of Vacuum Science & Technology B: Microelectronics and Nanometer Structures **8**, 1199 (1990).

[30] S.H. Zaidi D.S. Ruby, W.K. Schubert, J.M. Gee, Silicon cells made by self-aligned selective-emitter plasma-etchback process.

[31] S.H. Zaidi, D.S. Ruby, and J.M. Gee, IEEE Transactions on Electron Devices **48**, 1200 (2001).

[32] Y. Inomata, K. Fukui, and K. Shirasawa, Solar Energy Materials and Solar Cells **48**, 237 (1997).

[33] D.S Ruby, S.H Zaidi, S Narayanan, B.M Damiani, and A Rohatgi, Solar Energy Materials and Solar Cells **74**, 133 (2002).

[34] Jinsu Yoo, Gwonjong Yu, and Junsin Yi, Solar Energy Materials and Solar Cells **95**, 2 (2011).

[35] Päivikki Repo, Jan Benick, Ville Vähänissi, Jonas Schön, Guillaume von Gastrow, Bernd Steinhauser, Martin C. Schubert, Martin Hermle, and Hele Savin, Energy Procedia **38**, 866 (2013).

[36] Päivikki Repo, Antti Haarahiltunen, Lauri Sainiemi, Marko Yli-Koski, Heli Talvitie, Martin C. Schubert, and Hele Savin, IEEE Journal of Photovoltaics **3**, 90 (2013).

[37] D.H. Macdonald, A. Cuevas, M.J. Kerr, C. Samundsett, D. Ruby, S. Winderbaum, and A. Leo, Solar Energy **76**, 277 (2004).

[38] Yi-Fan Huang, Surojit Chattopadhyay, Yi-Jun Jen, Cheng-Yu Peng, Tze-An Liu, Yu-Kuei Hsu, Ci-Ling Pan, Hung-Chun Lo, Chih-Hsun Hsu, Yuan-Huei Chang, Chih-Shan Lee, Kuei-Hsien Chen, and Li-Chyong Chen, Nature nanotechnology **2**, 770 (2007).

[39] Th Her, Rj Finlay, and C Wu, Applied Physics Letters **73**, 1673 (1998).

[40] David G Cahill and Steve M Yalisove, MRS Bulletin **31**, 594 (2006).

[41] Michael a. Sheehy, Luke Winston, James E. Carey, Cynthia M. Friend, and Eric Mazur, Chemistry of Materials **17**, 3582 (2005).

[42] Rebecca Jane Younkin, Ph.D. thesis, Harvard University, 2001.

[43] J.F. Van Driel, H.M., Sipe, J.E. , Young, Physics review letters **49**, 1955 (1982).

[44] Experimental Results and Previous Models, Physical Review B **26**, 5366 (1982).

[45] H.M. Sipe, J.E., Young, J.F., Preston, J.S, van Driel, Physical Review B **27**, 1141 (1983).

[46] F. Keilmann and Y. H. Bai, Applied Physics A Solids and Surfaces **29**, 9 (1982).

[47] A. Y. Vorobyev, V. S. Makin, and Chunlei Guo, Journal of Applied Physics **101**, 034903 (2007).

[48] JoÌĹrn Bonse, Arkadi Rosenfeld, and JoÌĹrg KruÌĹger, Journal of Applied Physics **106**, 104910 (2009).

[49] S. HoÌĹhm, A. Rosenfeld, J. KruÌĹger, and J. Bonse, Journal of Applied Physics **112**, 014901 (2012).

[50] S. HoÌĹhm, A. Rosenfeld, J. KruÌĹger, and J. Bonse, Applied Physics Letters **102**, 054102 (2013).

[51] Claudia Wu, Ph.D. thesis, Harvard University, 2000.

[52] James Carey, Ph.D. thesis, Harvard University, 2004.

[53] E. Janzén, R. Stedman, G. Grossmann and H. G. Grimmeiss, Physical Review B **29**, 1907 (1984).

[54] Brion P. Bob, Atsushi Kohno, Supakit Charnvanichborikarn, Jeffrey M. Warrender, Ikurou Umezu, Malek Tabbal, James S. Williams, and Michael J. Aziz, Journal of Applied Physics **107**, 123506 (2010).

[55] C.W. Aziz, M. J., Tsao, J.Y., Thompson, M.O., Peercy, P.S., White, Physical review letters **56**, 2489 (1986).

[56] H. Okamoto, Materials Park: ASM International (2000).

[57] N.F. Mott, Canadian Journal of Physics **34**, 1356 (1966).

[58] Mark Thomas Winkler, Ph.D. thesis, Harvard University, 2009.

[59] Antonio Luque and Antonio MartÄś, Physical Review Letters **78**, 5014 (1997).

[60] William Shockley and Hans J. Queisser, Journal of Applied Physics **32**, 510 (1961).

[61] A. Araújo, G. L., Martí, Solar Energy Materials and Solar Cells **33**, 213 (1994).

[62] Jacob J. Krich, Bertrand I. Halperin, and AlaÌĄn Aspuru-Guzik, Journal of Applied Physics **112**, 013707 (2012).

[63] E. AntoliÌĄn, A. MartiÌĄ, J. Olea, D. Pastor, G. GonzaÌĄlez-DiÌĄaz, I. MaÌĄrtil, and A. Luque, Applied Physics Letters **94**, 042115 (2009).

[64] Mark T. Winkler, Daniel Recht, Meng-Ju Sher, Aurore J. Said, Eric Mazur, and Michael J. Aziz, Physical Review Letters **106**, 178701 (2011).

[65] Daniel Recht, Joseph T. Sullivan, Robert Reedy, Tonio Buonassisi, and Michael J. Aziz, Applied Physics Letters **100**, 112112 (2012).

[66] Yang Xia, Bangwu Liu, Jie Liu, Zenan Shen, and Chaobo Li, Solar Energy **85**, 1574 (2011).

[67] Bangwu Liu, Energy Procedia **38**, 289 (2013).

[68] MT Winkler, MJ Sher, and YT Lin, Journal of Applied Physics **111**, 093511 (2012).

[69] M. Halbwax, T. Sarnet, Ph. Delaporte, M. Sentis, H. Etienne, F. Torregrosa, V. Vervisch, I. Perichaud, and S. Martinuzzi, Thin Solid Films **516**, 6791 (2008).

[70] Vikram V. Iyengar, Barada K. Nayak, and Mool C. Gupta, Solar Energy Materials and Solar Cells **94**, 2251 (2010).

[71] SiOnyx Solar Achieves Record Results for Black Silicon Solar Cells, 2011.

[72] S. Kontermann, T. Gimpel, A.L. Baumann, K.-M. Guenther, and W. Schade, Energy Procedia **27**, 390 (2012).

[73] Rolf B Rendel, Japanese Journal of Applied Physics **44**, 4431 (2001).

[74] Stephen W. Bedell, Davood Shahrjerdi, Bahman Hekmatshoar, Keith Fogel, Paul a. Lauro, John a. Ott, Norma Sosa, and Devendra Sadana, IEEE Journal of Photovoltaics **2**, 141 (2012).

[75] Dong Seop Kim, Vijay Yelundur, Kenta Nakayashiki, Brian Rounsaville, Vichai Meemongkolkiat, Andrew M. Gabor, and Ajeet Rohatgi, Solar Energy Materials and Solar Cells **90**, 1227 (2006).

[76] Takao Yonehara, Kiyofumi Sakaguchi, and Nobuhiko Sato, Applied Physics Letters **64**, 2108 (1994).

[77] H. H. Li, Journal of Physical and Chemical Reference Data **9**, 561 (1980).

[78] Eli Yablonovitch and George D Cody, IEEE Transactions on Electron Devices 300 (1982).

[79] Vivian E Ferry, Marc A Verschuuren, M Claire Van Lare, Ruud E I Schropp, Harry A Atwater, and Albert Polman, Nano letters **11**, 4239 (2011).

[80] Peter Bermel, Chiyan Luo, Lirong Zeng, Lionel C Kimerling, and John D Joannopoulos, Optics express **15**, 16986 (2007).

[81] Dayu Zhou and Rana Biswas, Journal of Applied Physics **103**, 093102 (2008).

[82] Harry a Atwater and Albert Polman, Nature materials **9**, 205 (2010).

[83] Hairen Tan, Laura Sivec, Baojie Yan, Rudi Santbergen, Miro Zeman, and Arno H. M. Smets, Applied Physics Letters **102**, 153902 (2013).

[84] Vivian E Ferry, Marc a Verschuuren, Hongbo B T Li, Ewold Verhagen, Robert J Walters, Ruud E I Schropp, Harry a Atwater, and Albert Polman, Optics express **18**, A237 (2010).

[85] S. Pillai, K. R. Catchpole, T. Trupke, and M. a. Green, Journal of Applied Physics **101**, 093105 (2007).

[86] Benjamin G. Lee, Paul Stradins, David L. Young, Kirstin Alberi, Ta-Ko Chuang, J. Gregory Couillard, and Howard M. Branz, Applied Physics Letters **99**, 064101 (2011).

[87] Anastassios Mavrokefalos, Sang Eon Han, Selcuk Yerci, Matthew S Branham, and Gang Chen, Nano letters **12**, 2792 (2012).

[88] Ken Xingze Wang, Zongfu Yu, Victor Liu, Yi Cui, and Shanhui Fan, Nano letters **12**, 1616 (2012).

[89] K. Van Nieuwenhuysen, M. Récaman Payo, I. Kuzma-Filipek, J. Van Hoeymissen, G. Beaucarne, and J. Poortmans, Thin Solid Films **518**, S80 (2010).

[90] Rolf Brendel, Richard Auer, and Hans Artmann, Progress in Photovoltaics: Research and Applications **9**, 217 (2001).

[91] Jonathon Dore, Rhett Evans, Ute Schubert, Bonne D Eggleston, Daniel Ong, Kyung Kim, Jialiang Huang, Oliver Kunz, Mark Keevers, Renate Egan, Sergey Varlamov, and Martin A Green, Pregress in photovoltaics: research and applications **21**, 1377 (2013).

[92] D Amkreutz and J Mu, Progress in Photovoltaics: Research and Applications **19**, 937 (2011).

[93] Howard M. Branz, Charles W. Teplin, Manuel J. Romero, Ina T. Martin, Qi Wang, Kirstin Alberi, David L. Young, and Paul Stradins, Thin Solid Films **519**, 4545 (2011).

[94] Mark T. Sher, Meng-Ju, Winkler and Eric Mazur, MRS Bulletin **36**, 439 (2011).

[95] H Sshwartz, B., Robbins, J. Electrochem. Soc **123**, 1903 (1976).

[96] Satoshi Shimizu, Paul Stradins, Michio Kondo, and Akihisa Matsuda, Japanese Journal of Applied Physics **41**, L1297 (2002).

[97] K Sokolowski-Tinten, Physical Review Letters **81**, 224 (1998).

[98] J.E. Young, J.F., Preston, J.S., van Driel, H.M., and Sipe, Physical Review B **27**, 1155 (1982).

[99] Jeff F Young, J E Sipe, and H M Van Driel, Physical Review B **30**, 2001 (1984).

[100] Matthew J. Smith, Meng-Ju Sher, Benjamin Franta, Yu-Ting Lin, Eric Mazur, and Silvija GradecÌŇak, Journal of Applied Physics **112**, 083518 (2012).

[101] Benjamin G Lee, Howard M Branz, Yu-Ting Lin, Eric Mazur, and Meng-ju Sher, IEEE Photovoltaic Specialists Conference (2012).

[102] Stefaan De Wolf, Antoine Descoeudres, Zachary C. Holman, and Christophe Ballif, Green **2**, 1 (2012).

[103] M. Wolf, Proceedings of the Institute of Radio Engineerr **48**, 1246 (1960).

[104] W.T. Shockley, W. Read, Physcal Review **87**, 62 (1952).

[105] R.N. Hall, Physical Review **87**, 387 (1952).

[106] M. J. Keevers and M. a. Green, Journal of Applied Physics **75**, 4022 (1994).

[107] Antonio Luque and Antonio Martí, Advanced materials **22**, 160 (2010).

[108] Antonio Luque, Antonio Martí, Elisa Antolín, and César Tablero, Physica B: Condensed Matter **382**, 320 (2006).

[109] Peter D. Persans, Nathaniel E. Berry, Daniel Recht, David Hutchinson, Hannah Peterson, Jessica Clark, Supakit Charnvanichborikarn, James S. Williams, Anthony DiFranzo, Michael J. Aziz, and Jeffrey M. Warrender, Applied Physics Letters **101**, 111105 (2012).

[110] Brian R. Tull, Cynthia M. Friend, Michael a. Sheehy, and Eric Mazur, Materials Science and Engineering: B **137**, 289 (2007).

[111] Meng-ju Sher, Yu-ting Lin, Mark T Winkler, Eric Mazur, and Christian Pruner, Journal of Applied Physics **113**, 063520 (2013).

[112] James E Carey, Catherine H Crouch, Mengyan Shen, and Eric Mazur, Optics letters **30**, 1773 (2005).

[113] Mike Aziz, Metallurgical and materials transactions A **27A**, 671 (1996).

[114] MJ Aziz, Journal of Applied Physics **02138**, 1158 (1982).

[115] Jeff Y Tsao, J Aziz, and Michael O Thompson, Physical review letters **56**, 23 (1986).

[116] J.a. Kittl, M.J. Aziz, D.P. Brunco, and M.O. Thompson, Journal of Crystal Growth **148**, 172 (1995).

[117] Riccardo Reitano, Patrick M Smith, and Michael J Aziz, Journal of Applied Physics **76**, 1518 (1994).

[118] Taeseok Kim, Kirstin Alberi, Oscar D. Dubon, Michael J. Aziz, and Venkatesh Narayanamurti, Journal of Applied Physics **104**, 113722 (2008).

[119] D P Korfiatis, K-A Th Thoma, and J C Vardaxoglou, Journal of Physics D: Applied Physics **40**, 6803 (2007).

[120] A Rousse, C Rischel, S Fourmaux, I Uschmann, S Sebban, G Grillon, P Balcou, E Förster, J P Geindre, P Audebert, J C Gauthier, and D Hulin, Nature **410**, 65 (2001).

[121] Ellen J. Yoffa, Physical review B **21**, 2415 (1980).

[122] S K Sundaram and E Mazur, Nature materials **1**, 217 (2002).

[123] K. Sokolowski-Tinten, J. Bialkowski and D. von der Linde, Physical review B **51**, 14186 (1995).

[124] Niall Mangan, Ph.D. thesis, Harvard University, 2013.

[125] K. Sokolowski-Tinten and D. von der Linde, Physical Review B **61**, 2643 (2000).

[126] Pochi Yeh, *optical waves in layered media* (Wiley, CA, 1988).

[127] Jörn Bonse, Guillaume Bachelier, Jan Siegel, and Javier Solis, Physical Review B **74**, 134106 (2006).

[128] C. Shank, C. V., Yen, R., Hirlimann, Physical Review Letters **50**, 454 (2008).

[129] Yusaku Izawa, Shigeki Tokita, Masayuki Fujita, Mitsuo Nakai, Takayoshi Norimatsu, and Yasukazu Izawa, Journal of Applied Physics **105**, 064909 (2009).

[130] R.O. Cox-Smith, I. R.;Liang, H.C.;Dillon, Journal of Vacuum Science & Technology A: Vacuum, Surfaces, and Films **3**, 674 (1985).

[131] P Saeta, J Wang, Y Siegal, N Bloembergen, and E Mazur, Physical review letters **67**, 1023 (1991).

[132] B. Rethfeld, K. Sokolowski-Tinten, D. von der Linde, and S. Anisimov, Physical Review B **65**, 092103 (2002).

[133] K. Sokolowski-Tinten, J. Bialkowski, M. Boing, A. Cavaller and D. von der Linde, physical review B **58**, 805 (1998).

[134] Klaus Sokolowski-Tinten and Dietrich Von Der Linde, Journal of Physics: Condensed Matter **16**, R1517 (2004).

[135] C. W. Siders, Science **286**, 1340 (1999).

[136] Bryan C. Gundrum, Robert S. Averback, and David G. Cahill, Applied Physics Letters **91**, 011906 (2007).

[137] D. C. Thompson, M.O., Mayer, J. W., Cullis, A. G., Webber, H. C., Chew, N. G., Poate, J. M., Jacobson, Phys. Rev. Lett **50**, 896 (1983).

[138] J. D. Hoyland and D. Sands, Journal of Applied Physics **99**, 063516 (2006).

[139] Meng-Ju Sher, Ph.D. thesis, Harvard University, 2013.

[140] J. T. Sullivan, R. G. Wilks, M. T. Winkler, L. Weinhardt, D. Recht, a. J. Said, B. K. Newman, Y. Zhang, M. Blum, S. Krause, W. L. Yang, C. Heske, M. J. Aziz, M. BaÌĹr, and T. Buonassisi, Applied Physics Letters **99**, 142102 (2011).

[141] Antonio Martí, Antonio Luque, Nature photonics **5**, 137 (2011).

[142] B Tan and K Venkatakrishnan, Journal of Micromechanics and Microengineering **16**, 1080 (2006).

[143] K. von der Linde, D.; Sokolowski-Tinten, Applied surface science **154**, 1 (2000).

[144] H. Coster M.A. Bassam , P. Parvin , B. Sajad , A. Moghimi, Applied surface science **254**, 2621 (2008).